Assessing the retrieval procedure of complex-valued forces from airborne pressure fields by means of DIC-based full-field receptances in simplified pseudo-inverse vibro-acoustics

Alessandro Zanarini

Dynamics & Vibrations of Machines, DIN - Industrial Engineering Dept., University of Bologna, Italy

ARTICLE INFO

ABSTRACT

Lightweight structural components in many engineering fields can be severely excited by airborne pressure fields, becoming a concern for their structural dynamics and reliability. Nowadays, the quality reached by optical measurements, in contactlessly estimating - as maps of displacements over force - complex-valued full-field receptances, allows an accurate description of the structural dynamics in a broad frequency domain, without any numerical structural model. This is even more relevant for lightweight components, otherwise affected by potential distortions, coming from the inertia of more traditional transducers. High-speed DIC structural testing is here combined with acoustic propagation in direct and pseudo-invertable vibro-acoustic FRFs, obtained by the simple Rayleigh integral approximation, here re-formulated to take advantage of the experiment-based full-field receptances, when a force excites a vibrating surface, which radiates sound pressure into air and vice-versa. Starting from airborne pressure fields, known in their spectra, the pseudo-inverse vibro-acoustics aims at identifying the force, with a broad frequency band, which can be transmitted to the excitation locations, previously used in defining the vibro-acoustic FRFs in the direct problem. Extended details and considerations on this full-field receptance-based vibro-acoustic approximation are thoroughly provided, with special attention to its complex-valued nature, to numerical precision and to broad dynamics' excitation signature, thanks to the accurate DIC-based testing of a real thin plate.

1. Introduction

Any airborne broad frequency band pressure field - working on components as a distributed dynamic load - can boost the structural responses in reaching prohibitive operational motion states, especially in the case of lightweight assemblies, e.g., wings, fuselage or shields with a tight modal base inside the airborne pressure spectra. Furthermore, such excited structural dynamics can lead to a shorter life than expected, because of the higher levels reached in the strain-stress distribution of the specific realisation. The easiest examples that come to mind are certainly those of aircraft, wind turbines, high-speed vehicles and of space launchers, which are subjected to turbulence with broad dynamic signatures. In many NVH analyses, the simulations of the sound radiated by structural vibrations are obtained from simplified linear models [1–13], where many simplifying assumptions are made over

potential non-linearity, differences from the real manufacturing, damping, boundary conditions with potential related friction: the present experiment-based approach finds its motivations in avoiding all these simplifications. Sometimes similarly simplified approaches about the structural models are explicitly followed also in fluid-structure interaction simulations in the frequency domain, e.g., in [14–18]. In extensive fluid-structure interaction studies[1] more attention is generally paid to the fluid motion rather than seeking, but in fact disregarded, the best understanding of a structural part, with uncertainties, general damping (check [28,29]) and *complex-valued* ($\mathbb{C}$) eigenvectors; this because the experiment validation can become challenging [30–34], especially due to non-linearities in the fluid motion. In all these approximations, the structural model is not taken from any EFFMA, but simplified mostly by a *real-valued* ($\mathbb{R}$) truncated modal base from linear FEM, with the damping assumed only as proportional (check [28,29]), or totally disre-

[1] Although outside from the scope of this paper, see in details the many examples in this rich bunch [19–27], to prove the structural simplifications' recurrence, against a complex analysis of the fluid motion, therefore offering a path for future research.

Abbreviations

DIC	Digital Image Correlation	ODS	Operative Deflection Shape
dof	degree of freedom	SLDV	Scanning Laser Doppler Vibrometer
EFFMA	Experimental Full-Field Modal Analysis	ω	Circular frequency dependency
ESPI	Electronic Speckle Pattern Interferometry	$\mathbf{X_q}(\omega)$	Structural displacement map
FEM	Finite Element Modelling	$\mathbf{F_f}(\omega)$	Structural excitation forces
FRAC	Frequency Response Assurance Criterion	$H_{d_{qf}}(\omega)$	*Receptance* map
FRF	Frequency Response Function	$V_{af}(\omega)$	Vibro-Acoustic FRFs
MAC	Modal Assurance Criterion	$p(a_a, \omega)$	Sound Pressure Fields mapping
NDT	Non-Destructive Testing	$V_{fa}^+(\omega)$	Pseudo-inverse Vibro-Acoustic FRFs
NVH	Noise and Vibration Harshness	$\hat{F}_f(\omega)$	Identified Airborne Force

garded [35,36]. Instead, a key strength of this paper is the use of $\mathbb{C}$ FRFs to better replicate the real-life phenomena; therefore, proper operations follow the declaration of $\mathbb{C}$ quantities, otherwise to be intended simply as $\mathbb{R}$ ones. Also where the general damping is formulated [37–40] for the structural part, the simulations tend to neutralise it, returning to unverified models. Moreover, some investigations are focused only about a single tonal, or resonance, propagation [41], where just one eigensolution of the vibrating surface is used as the effective source of pressure fields. As confirmed also by the considerations of [42,43], this means that a lot of assumptions in simplified models may diverge from the real manufactured components, thus simulating something that might not be easily tuned, also with extended model updating [44–46]. The vibro-acoustical modal analysis, as pioneered – among others – in [47,48], can suffer the same FEM-related simplification issues, potentially adding identification errors, in particular due to modal model truncation and limited order [28,29], over the vibro-acoustic reciprocity, domain balance, symmetry and validity issues. As later explained, this paper will not be focused on any modal model – nor synthesis – to avoid the related errors, but instead on vibro-acoustic FRFs only.

A better representation of the real structural dynamics may come, instead, from experiment-based impedance models. The latter are here based on *receptance FRFs* [28,29], estimated in the framework of broad frequency band modal testing of manufactured and mounted components, when the lab excitations are close to operative loads; they are fully compatible with a modally dense structural dynamics of the components and with excitations, carrying complex patterns in their dynamic signatures. A viable and easily reproducible approach for pseudo-inverse vibro-acoustics is here sketched, based on a simple Rayleigh integral approximation, instead of more advanced specific approaches (e.g., [49–54], whose discussion is outside the scope of the paper). This procedure can be divided into steps: (i) exploring the direct interaction between the structural dynamics of the components and the diffused pressure fields, by pursuing the acoustic pressure mapping that is radiated from a vibrating surface; (ii) inverting that path for the structural responses due to the airborne acoustic pressure fields. It is like turning the vibrating plate into a flexible microphone, whose structural dynamics is described directly by testing *receptances*. In this way, the flexible surface, excited by the airborne pressure fields, gives back the excitation signal needed in the specific shaker head to obtain such ODSs, obtained from real testing, not from virtual structural models, hardly tuned.

The key-idea is therefore to use high spatial resolution *experiment-based full-field receptances* (*ebffr*), obtained from optical measurements, as the characterisation of the vibrating structure in the whole frequency domain of interest, without any specific assumption, except for the linearisation of the system dynamic behaviour around the operative loading conditions. In this way, the *ebffr* substitute any virtual model of the structural domain (e.g. FEM), therefore overtaking its complex tuning, because all the specifications of the materials, boundary conditions and loading patterns are already acquired from testing. Furthermore, *ebffr* add extreme detail - compared to more traditional lumped sensors like accelerometers or strain gauges [35] - in the spatial domain, being there-

fore able to carefully retain complex patterns in the ODSs without any inertia-related distortion.

Optical *native* full-field technologies, those based on an imaging sensor, approach the measurement, normally in denser grids than SLDV [55], from the point of view of the acknowledged spatial domain qualities, thanks to the continuity and consistency - among the neighbouring dofs - of the deflection field, as proved earlier by [56–58]. Among optical *native* full-field technologies, stroboscopic ESPI has given since the years 2000s [59,60] an extremely accurate displacement field, at each frequency of interest (even up to several kHz), but with prohibitive timings for broad frequency band testing. However, ESPI is more suited to controlled environments, typical of research projects [61,62]. High-speed DIC, available since around 2005 as early commercial prototypes, has good detail in the time resolved displacement maps, although the extraction of the correlated fields might be computationally intensive. However, in the frequency domain DIC can be more restricted, as the electronics bandwidth puts a trade-off among resolution, on-board storage and sampling rate, although nowadays relevant electronics improvements have been made. Furthermore, DIC technology has shown many in-situ applications [63–67], with much greater flexibility in non-controlled set-ups of wider industrial interest. Therefore, high-speed DIC is the optical *native* full-field technology here used for the dynamic testing of the vibrating surface.

The author started to investigate the potential of the growing full-field measurements in 2004-05 with the *Speckle Interferometry for Industrial Needs* project.[2] The early achievements[3] in the former were the basis for the fundamental research project TEFFMA,[4] which aimed at comparing the state-of-the-art in *native* (DIC, ESPI) full-field technologies with SLDV as reference, to explore if enhanced peculiarities can be provided to NVH applications by these experimental procedures, in progressive development. The first outcomes of TEFFMA were presented[5]
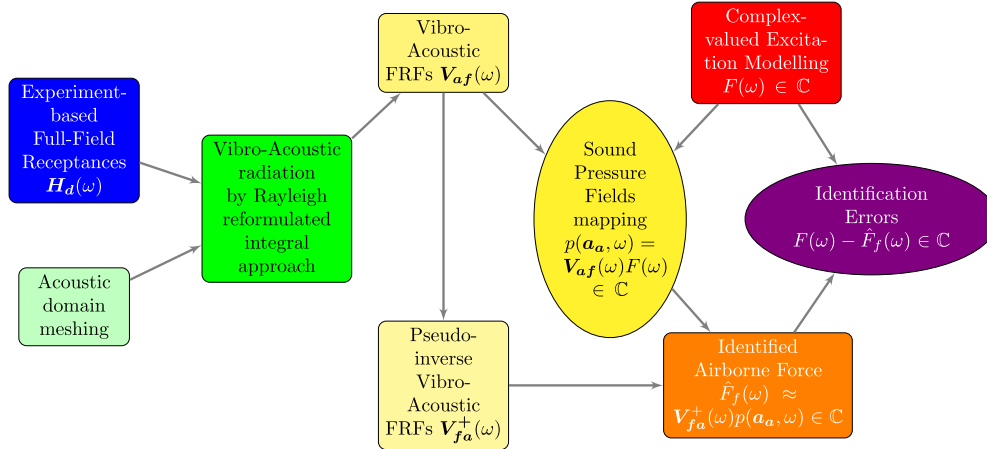
Fig. 1. Outlook of the steps for the accuracy assessment in pseudo-inverse airborne vibro-acoustic force identification.

in 2014, followed by consolidated reports[6] in 2015. In [61] a summary of the TEFFMA works was firstly attempted, while in [62] an extended description of the *ebffr estimation* was faced and in [46] the EFFMA was detailed with even stronger results than forecast by [68] together with full-field model updating attempts, based on modeshapes and resonance frequencies. In [69] the quality of *native* full-field datasets – especially ESPI and DIC – in broad frequency band dynamic testing was underlined. In [70] high resolution full-field rotational and strain FRFs were derived and compared. A risk index was formulated in [71–73] as a tool to identify the areas on components' surface that are exposed to failure due to dynamic loadings, with special care to the acceptance threshold of potential defects [74,75]. The use of the TEFFMA project's *ebffr* started to be extended to vibro-acoustics in [76,77] for sound radiation field approximations by means of ESPI-based testing, in [78] by reduced DIC-based dataset, while in [79] the effect of errors on vibro-acoustics from SLDV *ebffr* was investigated. The author has shown how the growing *native* full-field techniques have started to offer interesting development paths, thanks to their data fields' consistency and continuity, with clear repercussions in EFFMA[7] and model updating, vibro-acoustics[8] and several derivative evaluations (rotational dofs[9], strains, stresses, risk index maps[10]). The enhanced assessment of the structural dynamics and of the fatigue life predictions by spectral methods were possible thanks to the coherent and hyper-detailed mapping about the local behaviour, coming from full-field optical techniques, which was a clear advantage since the ESPI-related testing researches. The attention to high-cycles fatigue - from dynamic loading and vibrations - is clearly in the background of this paper as future research enhancement, because the airborne sound pressure field can be seen as distributed loading, therefore interwoven with NDT & risk grading procedures.

The accuracy of the *pseudo-inverse vibro-acoustic full-field experiment-based* procedure – the core for the retrieval of airborne $\mathbb{C}$ forces – is here investigated by following the scheme in Fig. 1. In the latter, the DIC-based *ebffr* cooperate with the acoustic domain meshing to obtain the *direct vibro-acoustic FRFs*, from which the *pseudo-inverse vibro-acoustic FRFs* are estimated as detailed in Section 2. By means of $\mathbb{C}$ excitation modelling, the *direct vibro-acoustic FRFs* give the mapping of the sound pressure fields. To test the suitability of the airborne force identification procedure, the calculated sound pressure fields are fed back to the *pseudo-inverse vibro-acoustic FRFs*, to obtain the identified airborne force and the identification errors. Specifically, a recall of the *ebffr* testing in the TEFFMA project is sketched as Section 2.1, with attention to DIC's calibration procedure for optimal *ebffr* quality. To address the *direct* vibro-acoustic modelling, the Rayleigh integral formulation is re-elaborated in Section 2.2 from [1–3,6–11,13] to obtain the *vibro-acoustic transfer matrices*, but with the aid of *ebffr*, instead of any other numerical model of the structure (e.g., finite or boundary elements, wave-based or any functional expansion). Notes are added for the *pseudo-inverse* vibro-acoustic analyses of the identified force from airborne acoustic pressure fields and *ebffr*, inspired by the same background as in [83–85]. Section 2.3 is dedicated to represent any signal, from the simpler noise-free $\mathbb{R}$ excitation to the more adherent signal to natural excitation, like $\mathbb{C}$ signals with randomness in the *complex amplitude* and *phase*.

Section 3 contains all the simulations of the *direct* and *pseudo-inverse* vibro-acoustic problem – obtained from DIC-based high spatial resolution *ebffr*, with examples commented in the space and frequency domains. Section 3.1 anticipates notes on the acoustic domain's meshing, for high spatial resolution results in the *vibro-acoustic transfer matrix* in Section 3.2. Special attention is given to the contribution of the *ebffr* maps and to the multi-modal superposition, also manifest far from the eigenfrequencies, in obtaining accurate radiated *acoustic pressure spectra* and *pressure fields* in Sections 3.3 and 3.4, both evaluated while varying the excitation model in Section 2.3. The *pseudo-inverse vibro-acoustic FRFs* are investigated in Section 3.5, to detail in Section 3.6 the identification of the force, induced by the modelled airborne pressure fields in the *direct* problem, on the structural location of the shaker in *ebffr* testing. Section 3.7 gives further comments and explanations about the proposed simulations. In Section 3.8 a brief procedure's validation outlook is proposed for future works.

The reader's attention is drawn to Section 4 for the final conclusions.

2. Materials and methods

A recall of the *ebffr* formulation is given in Section 2.1, together with descriptions about the testing procedures, the set-up, the stereo vision calibration and DIC measurements. The *experiment-based full-field*

---

[6] In Proceedings of the ICoEV2015 International Conference on Engineering Vibration, Ljubljana, Slovenia, September 7-10, Univ. Ljubljana & IFToMM, 2015, symposium *Full Field Measurements for Advanced Structural Dynamics*: Model updating from full field optical experimental datasets; Comparative studies on full field FRFs estimation from competing optical instruments; Accurate FRFs estimation of derivative quantities from different full field measuring technologies; Full field experimental modelling in spectral approaches to fatigue predictions.

[7] See specifically [46,59,61,62,69,70] for enhancements in full-field structural dynamics and model updating.

[8] See specifically [76–79] for vibro-acoustics.

[9] In [61,70] the reader can specifically appreciate the effect of noise in the full-field measurements for the estimation of rotational dofs, which are fundamental in building reliable hybrid models for complex structures [28,29,44,80–82].

[10] See instead [71–75] for full-field mapping in fatigue predictions and failure risk grading by spectral methods.
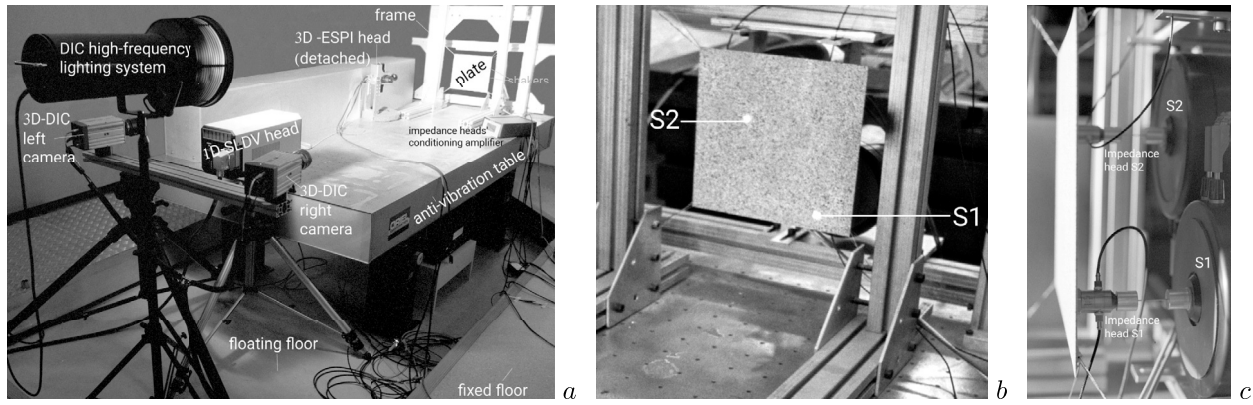
Fig. 2. Overview of the test-rig in the TEFFMA project (see [46,61,62,69,70]) in *a*, focus on the restrained plate sample with highlighted shakers' locations in *b* and on the 2 shakers, on the back of the plate with their impedance heads, in *c*.

re-elaboration of the Rayleigh integral approximation for the *direct* and *pseudo-inverse* vibro-acoustic analyses is done in Section 2.2. The formulation of dynamic signatures in excitation forces is summarised in Section 2.3.

2.1. Full-field experiment-based modelling by means of receptance FRFs

In the TEFFMA project at TU-Wien, the following research aids were available[11]: coexistence of SLDV, Hi-Speed DIC and stroboscopic ESPI, as *optical full-field* measurement techniques; a dedicated room for low vibrations' assessment with ground insulation by a seismic floor and an optical table; vibrations & modal analysis general testing means. Precise assessments on the technological limits of each instrument were run, to achieve the best compromise for the concurrent application of all techniques in a common set-up. The set-up arrangement that emerged, for the comparative *full-field FRF estimation* from the 3 different optical technologies, was unique as in Fig. 2: in the frequency range of [20-1024] Hz, thanks to a proper tuning, a working overlapping of performances was obtained. The resulting datasets from each technology were not precisely super-imposable at the simple level of raw output, released by the proprietary software, although highly promising for *qualitative* comparisons. Therefore, topology transforms were added whenever needing the datasets in the same physical references for appropriate *quantitative* comparisons of the *receptance* matrices $H_d(\omega)$, but not here, due to the use of only one technology, not to add further noise.

2.1.1. Mathematical basics for full-field receptances

In [28,29] the definition of *receptance* matrix $H_{d_{qf}}(\omega)$ is given among the FRFs of output displacements in *q*-dofs over input forces in *f*-dofs, under the assumption of noise only in the output (H1 estimator). This relation can be extended to *full-field FRF estimation* for the experiment-based description of the structural dynamics of a component in testing. 2 shakers were here used for multiple – mutually exclusive – excitations, while *many*-output responses were collectable in the whole frequency domain. In the following expression:

$$H_{d_{qf}}(\omega) = \frac{\sum_{m=1}^{N} S_{X_q F_f}^{m}(\omega)}{\sum_{m=1}^{N} S_{F_f F_f}^{m}(\omega)} \in \mathbb{C}, \tag{1}$$

$X_q \in \mathbb{C}$ is the output displacement at *q*-th structural dof induced by the input force $F_f \in \mathbb{C}$ at *f*-th dof; $S_{X_q F_f}^{m}(\omega)$ is the *m*-th cross-power spectral density between input and output; $S_{F_f F_f}^{m}(\omega)$ is the *m*-th auto-power spectral density of the input; N is the number of repetitions.

2.1.2. General notes on the test rig

In the TEFFMA project, the sample was a thin aluminium rectangular plate (dimensions: 250 x 236 x 1.5 mm, flat), fixed by metal ropes - to restrain any excessive rigid-body movement - to a rigid frame, the latter bolted on the insulating air-spring optical table (see Fig. 2b). The set-up was designed to let the lightweight structure retain a modally dense and complex structural dynamics, keeping unsimplified constraints and damping distribution. A non-structural layer of paint, with a pattern of random noise for DIC, was sprayed on the front-side of the plate. The two shakers of Fig. 2c gave, separately, excitations on the back-side of the plate, to fulfil the ESPI stepped-sine phase-shifting proprietary acquisition procedures, driven by an external waveform generator; instead, LMS Test.Lab system managed the shakers for SLDV and DIC acquisitions. Impedance heads (see them in Fig. 2c), used to estimate the *receptance* FRFs $H_d(\omega)$ of Eq. (1), sampled the force signals at the interfaces between shakers and plate.

2.1.3. Estimating full-field FRFs from high-speed DIC

As can be see in Fig. 2a, the Dantecdynamics Q-450 Hi-Speed DIC stereo system, from year 2008, in TEFFMA tests (see [62] for more details) had a dedicated high intensity & high frequency white lighting system. On each of the 2 high-speed cameras (Nanosense Mk III), 4 GB of on-board memory were installed: this permitted to record 2 s-long time-histories and to achieve 2048 frames-per-seconds (fps) at the image resolution of 640×512 pixels. A professional-grade macro-photography lens (Nikon AF Micro Nikkor 60 mm f2.8 D) was mounted on each camera for optimal vision integrity.

With optical techniques specific attention should be dedicated to the camera system calibration, which is sometime underestimated, whereas it can play a relevant role in assuring high-quality measurements. In TEFFMA testing the calibration was done with multiple views of a dimensionally-known target, a planar chequered board. To give the reader the basics of the calibration procedure, an example of a chequered pattern is given in Fig. 3a. The target has a randomly chosen pose for each view in front of the epipolar geometry of the stereo camera vision to be calibrated. Perspective projections and real lens distortions need to be evaluated in the optimisation of the *intrinsic* and *extrinsic* parameters of each freely-posed camera, which might be different from the idealised pinhole camera behaviour.[12] In each camera C, features of the

---

[12] In [86] the *intrinsic* parameters are grouped into $\alpha_C = (f_{x_C}, f_{y_C}, s_C, u_{P_C}, v_{P_C}, k_{1_C}, k_{2_C}, k_{3_C}, p_{1_C}, p_{2_C})$, where f_{x_C}, f_{y_C} are the camera focal lengths in image plane directions, s_C is the pixel skewness, u_{P_C}, v_{P_C} are the coordinates of the principal point as in Fig. 3a; instead, in the image distortion polynomial modeling, $(k_{1_C}, k_{2_C}, k_{3_C})$ are used for the radial – and (p_{1_C}, p_{2_C}) for the tangential – distortions of the optical/camera system. See [86,87] for the procedure linked to the more standard camera/lens models from the pioneering [88,89], see [90] for lens distortion advanced modelling. The *extrinsic* parameters $\beta_C = [R_C, T_C]$ define the pose of the camera system into the world reference system, where R_C is a
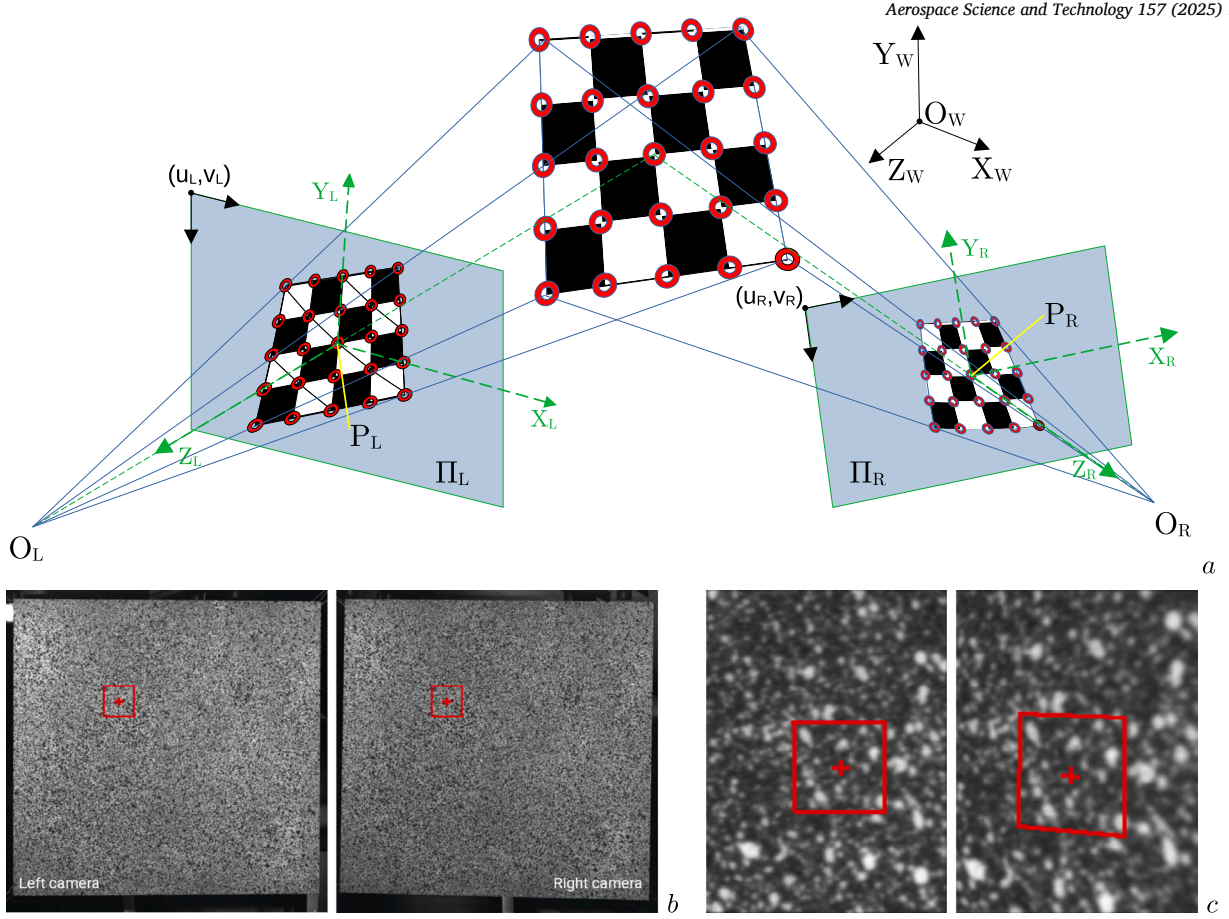
Fig. 3. Schematic of the main steps in DIC measurements. In *a* the epipolar geometry is displayed in the stereo vision camera calibration by a chequered pattern with highlighted (red circles) corner features on distorted perspective projections: the reference systems $(X, Y, Z)_{L,R,W}$ are added for the left (L) & right (R) cameras and for the 3D world (W) with centres P_L, P_R and O_W; each optical system/camera centre $O_{L,R}$ projects at $(u_{P_{L,R}}, v_{P_{L,R}})$ in the principal point $P_{L,R}$ on the image plane $\Pi_{L,R}$ with 2D coordinates $(u_{L,R}, v_{L,R})$ starting at the upper-left corner; each camera system has a specific focal length $f_{L,R} = \|O_{L,R} - P_{L,R}\|$. In *b*, after the calibration of the stereo vision system, an example of rectified images' pair is proposed for facet correlation. In *c* an exaggerated example of facet deformation & motion tracking in successive steps of the rectified time histories is shown. (For interpretation of the colours in the figure(s), the reader is referred to the web version of this article.)

dimensionally known pattern (e.g., the corners highlighted by red circles in Fig. 3a) are tracked in the image plane at multiple poses to identify the *intrinsic* parameters in an optimisation strategy, here driven by the Istra4D proprietary software (version 4.2.2.79, with null pixel skewness s_C and third radial distortion coefficient k_{3_C}). The same series of feature points is later used in a second optimisation of the whole stereo vision system to extract the *extrinsic* parameters of each camera, while defining a unique world coordinate reference system for the following measurements in the test. A new calibration is needed whenever the parameters of the optical set-up are changed. Special care was used in the TEFFMA lab to minimise the errors of both the calibration steps, to increase the fidelity of each 3D contour reconstruction, as can be seen in Table 1.

In DIC, as shown in Fig. 2b or Fig. 3b, a high-contrast random pattern is applied on the deforming surface (see [91,92] for the processing parameters' and pattern's selection), illuminated by white light. Light intensity patterns, back scattered from the specimen, are recorded by the cameras in series of *raw* images. By means of the *intrinsic* parameters from the calibrated stereo vision, the *rectified* images are obtained from the *raw* series. As in [93], motion magnification techniques may try to further improve the displacement detection from the *rectified* images, before the core *image correlation* begins. In DIC processing, in each synchronised pair of *rectified* images, like in Fig. 3b as obtained at a spe-

cific time step, the whole 2D domain of random intensities is divided into overlapping facets, whose center is the final structural *q*-th dof. A facet pair of the stochastic pattern is correlated by DIC algorithms (see [94,95] for basic concepts) in each camera – finding its position on the image planes Π_L, Π_R as in Fig. 3a – to reconstruct the 3D contour of the measured field with the *extrinsic* parameters, where the calibration accuracy is of great relevance. Each facet is also tracked along the *rectified* time-series, like in Fig. 3c, to evaluate the transformations due to the dynamics or loading. The displacement field – recorded in the final *correlated* datasets at specific time instants – at each step is obtained by the contour differences from the previous step.

The DIC-based *ebffr* datasets here used contain $N_q = 11988$ dofs ($N_q = 111 \times 108$, around 2.25 mm structural grid spacing), obtained from 520×512 pixel sized images and 19×19 pixel facet size with 50% overlapping in DIC algorithms. There are 2008 frequency lines, with a frequency space of 0.5 Hz in the [20-1024] Hz frequency range, thanks to 2 s at 2048 fps as acquisition parameters, retaining 20 Hz as the minimal frequency constraint from the ESPI technique. In each of the 4096 image pairs at every repetition, the displacements from the previous step were evaluated as 3D field (only meaningful in the out-of-plane direction), in the reference system, to fill the time-histories, later transformed – together with the force signal – into the frequency domain for the FRF evaluation of Eq. (1), with $N = 20$ for DIC. The datasets were obtained separately from 2 shakers in different energy injection locations.

Note that the DIC-based datasets are not interpolated, therefore adding no computing noise from any topology transform. The *direct* and

---

3×3 rotational matrix from angles $[\theta_{1_C}, \theta_{2_C}, \theta_{3_C}]$ and T_C a 3×1 translational vector with components $[t_{1_C}, t_{2_C}, t_{3_C}]$.

Table 1

Relative residual errors – evaluated as optimisation residuals errors against the identified quantity – in the DIC stereo camera system calibration for the TEFFMA project. The high err.$t_{1_{Left}}$ comes from a finite residual – in the same magnitude as for the other components – against a minimal identified value.

Camera	err.f_{x_c}	err.f_{y_c}	err.u_{P_c}	err.v_{P_c}	err.k_{1_c}	err.k_{2_c}	err.p_{1_c}	err.p_{2_c}
C=Left	9.211e-05	1.001e-04	4.306e-03	5.392e-03	-7.347e-02	5.773e-02	-2.366e-02	2.120e-01
C=Right	9.328e-05	1.040e-04	3.595e-03	6.659e-03	-3.045e-02	3.028e-02	-1.735e-02	-7.076e-02

Camera	err.θ_{1_c}	err.θ_{2_c}	err.θ_{3_c}	err.t_{1_c}	err.t_{2_c}	err.t_{3_c}
C=Left	1.810e-04	-5.318e-03	4.760e-03	-2.845e+01	2.689e-02	2.117e-04
C=Right	1.729e-04	-7.093e-03	-2.458e-03	4.972e-02	1.162e-02	2.126e-04

pseudo-inverse vibro-acoustic analyses take full advantage of the higher spatial resolution in raw DIC-based *receptances*, in order to appreciate high-speed DIC - at its best - in the test-based description of the vibrating surface's dynamic behaviour. Instead, in [78] the author briefly used, for the first time, DIC-based *ebffr* in the *pseudo-inverse* vibro-acoustic simulations, but those were interpolated at the moderate resolutions of SLDV [79].

2.2. Simplified formulation of the direct & pseudo-inverse vibro-acoustic problem

In order to increase the reproducibility of the DIC-based achievements, a simplified vibro-acoustic formulation is exploited for flat surfaces, in the wake of the Rayleigh integral approximation. 3D *ebffr* datasets might be proficiently used also in more advanced acoustic simulation methodologies for manifold vibrating surfaces. The whole formulation is here re-interpreted and coded in C-programming language. The idea is to focus the attention only to the pressure induced in the medium by the vibrating plate, therefore any medium motion is excluded. Other pressure sources might be later superimposed. In the acoustic domain A, or air, each a-th acoustic dof has global coordinates a_a. According to [1–3,6–11,13] in the case of propagating waves in a medium at rest, the Helmholtz equation can define the sound pressure $p(a_a, \omega)$ as:

$$p(a_a, \omega) = 2i\omega\rho_0 \int_S v_n(q_q, \omega)G(r_{aq}, \omega)dS \in \mathbb{C}, \qquad (2)$$

where i is the imaginary unit, ρ_0 is the medium (air) density, $v_n(q_q, \omega)$ is the normal (out-of-plane) velocity of the infinitesimal vibrating surface dS located in the global coordinate q_q, q representing the whole vector of coordinates of the vibrating surface S or structural domain. The free-space Green's function $G(r_{aq}, \omega)$ is defined by:

$$G(r_{aq}, \omega) = \frac{e^{-ikr_{aq}}}{4\pi r_{aq}} = \frac{e^{-i\omega r_{aq}/c_0}}{4\pi r_{aq}} \in \mathbb{C}, \qquad (3)$$

with $k = \omega/c_0 = 2\pi/\lambda$ as the wavenumber in the Helmholtz equation (c_0 is the speed of sound at rest in the medium, λ is the acoustic wavelength), with $r_{aq} = \|r_{aq}\|$ as the norm of the distance $r_{aq} = a_a - q_q$ between the locations in the acoustic and structural domains.

2.2.1. Direct vibro-acoustic formulation with full-field receptances

The relation $v_n(q, \omega) = i\omega X_n(q, \omega)$ gives the normal velocities $v_n(q, \omega) \in \mathbb{C}$ (over the static configuration q) in the frequency domain from the out-of-plane displacements $X_n(q, \omega) \in \mathbb{C}$. The latter can be retrieved by $X_n(q, \omega) = H_{d_nqf}(\omega) \cdot F_f(\omega)$, where the *receptance FRFs* $H_{d_nqf}(\omega)$ from Eq. (1) are of size $N_q \times N_f$ - being N_q the number of the outputs and N_f of the inputs - and the *excitation signatures* $F_f(\omega) \in \mathbb{C}$ are of size N_f. The structural domain S, which scatters the sound pressure, can be approximated as $S \approx \sum_q \Delta S_q$ – where ΔS_q is the discretisation of the finite area around the q-th dof in q_q – to rewrite Eq. (2) as:

$$p(a_a, \omega) \approx -2\omega^2\rho_0 \sum_q^{N_q} H_{d_nqf}(\omega)F_f(\omega)G_{aq}(r_{aq}, \omega)\Delta S_q \in \mathbb{C}. \qquad (4)$$

A *diffusion matrix* $T_{aq}(\omega) \in \mathbb{C}$ can be defined with element $T_{aq}(\omega) = -2\omega^2\rho_0 G_{aq}(r_{aq}, \omega)\Delta S_q \in \mathbb{C}$, sized $N_a \times N_q$, because $G_{aq}(r_{aq}, \omega)$ and ΔS_q are functions of the locations of the N_a discrete points in the acoustic domain and of the N_q points on the structure. By using $T_{aq}(\omega)$, Eq. (4) becomes:

$$p(a_a, \omega) \approx T_{aq}(\omega)H_{d_nqf}(\omega)F_f(\omega) \in \mathbb{C}. \qquad (5)$$

The *vibro-acoustic transfer matrix* $V_{af}(\omega)$, sized $N_a \times N_f$, can be defined here as *vibro-acoustic FRFs* between the *structural forces* and the *acoustic pressures* as:

$$V_{af}(\omega) = T_{aq}(\omega) \cdot H_{d_nqf}(\omega) \in \mathbb{C}, \qquad (6)$$

to compact Eq. (5) into Eq. (7), which maps the acoustic pressure fields, particularly useful when the vibro-acoustic system of Eq. (6) is kept unchanged and only the excitation signature varies:

$$p(a_a, \omega) \approx V_{af}(\omega)F_f(\omega) \in \mathbb{C}. \qquad (7)$$

Note that the *vibro-acoustic transfer matrix* $V_{af}(\omega)$ has not the same formulation found for the so-called *acoustic transfer vectors*, instead defined in [7,84,96] between the *surface velocities* and the *acoustic pressures*, because now $V_{af}(\omega)$ carries the $\mathbb{C}$ structural dynamics by means of the whole *ebffr*.

2.2.2. Indirect vibro-acoustic formulation and excitation force retrieval from sound pressure fields

Eq. (7) can be reversed, to obtain the estimation of the forces $\hat{F}_f(\omega)$, which are induced, by known pressure fields $\hat{p}(a_a, \omega) \in \mathbb{C}$ acting on the structure, at the known excitation/shaker locations q_f of the *ebffr*:

$$\hat{F}_f(\omega) \approx V_{fa}^+(\omega)\hat{p}(a_a, \omega) \in \mathbb{C}, \qquad (8)$$

with the *pseudo-inverse* of $V_{af}(\omega)$ of Eq. (6) as in [83–85], sized $N_f \times N_a$, here symbolised as $V_{fa}^+(\omega)$, also callable as *acoustic-vibrational FRFs matrix* between the *acoustic pressures* and the *forces* on the structure with its dynamics, and given by:

$$V_{fa}^+(\omega) = [V_{fa}^H(\omega)V_{af}(\omega)]^{-1}V_{fa}^H(\omega) \in \mathbb{C}, \qquad (9)$$

with $()^H$ as the Hermitian operator. Note that the inversion of a frequency dependent $\mathbb{C}$ matrix can be source of conditioning issues and to be made at each angular frequency ω. However, the inversion of the $\mathbb{C}$ square matrix $V_{fa}^H(\omega)V_{af}(\omega)$, of size $N_f \times N_f$, can be greatly simplified when N_f is very small or unity, the latter turning the operation into a basic problem.[13]

---

[13] As it will be used later in this paper, the many *vibro-acoustic FRFs* are here evaluated from only *one* excitation at a time, avoiding numerical matrix inversion issues, because the $\mathbb{C}$ square matrix $V_{fa}^H(\omega)V_{af}(\omega)$ is reduced to a $\mathbb{C}$ scalar, therefore with a very basic algebraic evaluation. Nonetheless, as the conditioning of the pseudo-inversion of FRF-matrices receives attention in literature, it might be stated that the high quality [62,69] of the *many* optical full-field *receptances* – and related *Coherence functions* – gives a tangible contribution to avoid in these datasets bad output locations and, according to [96,97], to improve the pseudo-inversion as a over-determined case even in multi-input conditions (not here), also thanks to the well-known topology of the inputs

If the evaluated pressure field of Eq. (7) is used to feed Eq. (8), $p(a_a, \omega) \equiv \hat{p}(a_a, \omega)$, the quality of the airborne force identification process can be easily assessed by the error function $Err_{F_f}(\omega)$, between the original excitation $F_f(\omega)$ and the identified airborne force $\hat{F}_f(\omega)$:

$$Err_{F_f}(\omega) = F_f(\omega) - \hat{F}_f(\omega) \in \mathbb{C}. \tag{10}$$

2.3. Formulation of dynamic signatures in excitation forces

Different excitation signatures for the components of $F(\omega) \in \mathbb{C}$ (*real* $F_r(\omega)$ and *imaginary* $F_i(\omega)$ parts) are here discussed, in order to appreciate the contribution of *ebffr*, thanks to their numerical representation, more adherent to real-life structural dynamics. Coloured noises, being described by the $1/\omega^\alpha$ factor, are selected to be the general shape of the amplitude-modulated forces, with $\alpha \in [-2, 2]$ indicating the specific *noise colour*: $\alpha = -2$ for *violet*, $\alpha = -1$ for *blue*, $\alpha = 0$ for *white*, $\alpha = 1$ for *pink* and $\alpha = 2$ for *red noise*. The following shared quantities can be defined in all the mathematical formulations later used in Eqs. (11)-(14): F_0 is the reference amplitude for the modulation; S_0 is the sinusoidal phase range multiplier; N_p is the number of half cycles of the phase in the range; ω_0 is the starting frequency; $\Delta\omega$ is the frequency range; θ_0 is a reference phase; $\theta(\omega) = S_0 \sin(\pi N_p(\omega - \omega_0)/\Delta\omega + \theta_0)$ is a selected phase function; β_{F_0}, being $0 \le \beta_{F_0} \le 1$, is the level of randomness in the amplitude; $Rand_{F_0}$, $Rand_\theta$ are functions returning a pseudo-random number in the range 0 to 1; β_θ is the level of randomness in the phase. For all the examples in Section 3, these common values were fixed: $F_0 = 0.050$ N, $S_0 = 1.0$ rad, $N_p = 2$, $\theta_0 = 0.5\pi$ rad, $\beta_{F_0} = 0.05$, $\beta_\theta = 0.15/\pi$.

2.3.1. Real-valued coloured noise

The excitation $F(\omega)$ can be defined as a $\mathbb{R}$ *coloured noise* if:

$$F_r(\omega) = \frac{F_0}{\omega^\alpha}, \qquad F_i(\omega) = 0, \qquad F(\omega) = \left[F_r(\omega), F_i(\omega) \right] \in \mathbb{C}. \tag{11}$$

Each frequency line component has the same phase, simply put to zero phase lag by the null imaginary component $F_i(\omega)$. This type of noise is labelled "std", for its *standard* formulation, as can be found in Figs. 8, 12, 17 and 18, and was the only simple type previously used by the author in [61,71–74,76–78].

2.3.2. Complex-valued coloured noise

The excitation $F(\omega)$ can be defined as a $\mathbb{C}$ *coloured noise* if:

$$F(\omega) = \frac{F_0}{\omega^\alpha} e^{i\theta(\omega)} \in \mathbb{C}, \tag{12}$$

with $\theta(\omega)$ to address the varying phase with a specific function. This type of noise is labelled "sp", for its *sinusoidal phase* formulation, as can be found in Figs. 9, 13, 19 and 20.

2.3.3. Real-valued coloured noise with random amplitude variations

The excitation $F(\omega)$ can be defined as a $\mathbb{R}$ *coloured noise with random amplitude variations* if:

$$F_r(\omega) = \frac{F_{0_r}}{\omega^\alpha}, \qquad F_i(\omega) = 0, \qquad F(\omega) = \left[F_r(\omega), F_i(\omega) \right] \in \mathbb{C}. \tag{13}$$

Here $F_{0_r} = F_0(1 + \beta_{F_0}(Rand_{F_0} - 0.5))$, in which F_0 is the mean – or reference – amplitude, upon which are added random variations. This type of noise is labelled "ra" for its *random amplitude* – but zero phase lags – formulation, as can be found in Figs. 10, 14, 21 and 22.

2.3.4. Complex-valued coloured noise with random amplitude & phase variations

The excitation $F(\omega)$ can be defined as a $\mathbb{C}$ *coloured noise with random amplitude & phase variations* if:

$$F(\omega) = \frac{F_{0_r}}{\omega^\alpha} e^{i\theta_r(\omega)} \in \mathbb{C}. \tag{14}$$

As above, $F_{0_r} = F_0(1 + \beta_{F_0}(Rand_{F_0} - 0.5))$, where F_0 is the reference for the amplitude randomness. Also, $\theta_r(\omega) = \theta(\omega)(1 + \beta_\theta(Rand_\theta - 0.5))$ with $\theta(\omega)$ as the chosen phase function, with the addiction of random phase variations. This type of noise is labelled "rap" for its *random variations* in the *amplitude* and *sinusoidal phase* formulation, as can be found in Figs. 11, 15, 23 and 24.

Note how this signal replicates the shape of any experiment-based force acquisition, with a generically varied spectrum. Therefore, in these approaches based on *ebffr*, any testing force can be retained with its real-life components, without assumptions nor compromises, except the respect of the linearity relation between forces and structural responses.

3. Results and discussion

Examples with DIC-based *full-field receptances* are discussed in the following subsections to underline how the reliable estimation of the *vibro-acoustic transfer matrix* $V_{af}(\omega)$ in Eq. (6) can be of relevance, also for the *pseudo-inverse* $V_{fa}^+(\omega)$ in Eq. (9). From Section 2.3 the excitation signatures are taken, to evaluate the acoustic pressure in Eq. (7) and to retrieve the airborne force in Eq. (8). The arrangement of the proposed simulations is here sketched as follows. Section 3.1 is devoted to briefly clarify the terms of the vibro-acoustic simulations. In the *direct vibro-acoustic* analyses, as depicted in Table 2, Section 3.2 evaluates the $V_{af}(\omega)$ in a single acoustic dof with broad frequency range and in the whole acoustic mesh at three specific frequencies. Section 3.3 deals instead with the $p(a_a, \omega)$ spectra, obtained from the specific coloured noises. Section 3.4 comments what obtained on the $p(a_a, \omega)$ fields, by means of the same coloured noises. In the *indirect*, or *pseudo-inverse*, *vibro-acoustic* analyses, as depicted in Table 3, Section 3.5 evaluates the $V_{fa}^+(\omega)$ from a single acoustic dof towards the structural dof of shaker 1. Section 3.6 deals instead with the retrieval of $\hat{F}_{S1}(\omega)$ spectra as in Eq. (8), obtained from the specific coloured noises, and of the related errors $Err_{F_{S1}}(\omega)$ as in Eq. (10). Section 3.7 gives a global discussion for the presented results, while in Section 3.8 further ideas are given for future extensions and new research works.

A few notes explain the directives taken in the 2D graphs and 3D $\mathbb{C}$ maps of this Section. For the 2D graphs, in the centre at the top, the sketched main function is reported by the magenta title, the same colour being used also for the acoustic dof of inquiry on the grey-toned 3D maps. The label "RR", or "_r", indicates, in all the evaluations, the use of *raw receptances*, therefore not further processed by any tool. At the top left, in dark yellow appears the frequency line of interest, as well as the corresponding vertical line in the graphs, like a frequency cursor. Just below are written the involved functions/parts (in red), with the values at the specific frequency; in the graphs appears a corresponding horizontal red line. Grey text, positioned on the right side, is used to annotate the extremes of the main function (red curve) and the quantity's descriptor. When a secondary function is needed, it is sketched in the graph as a black curve; also its values, at the specific frequency, and its descriptor are reported in black text, at the top left of the graph's subframes (*complex amplitude* and *phase*); no horizontal black line is added. The extremes of the frequency range are just below the frame of the graph. The references of the dataset (for geometry and frequency) appear in grey text, on the left side, at the bottom of the graphs, confirming

---

& outputs. Furthermore, Singular Value Decomposition (SVD) is suggested in [96,98] to improve the conditioning of the pseudo-inversion, or of the weighted pseudo-inversion as in [99,100], specifically around resonances, reminding that the Acoustic Transfer Matrix (ATM) as defined in [96] is a different quantity than $V_{af}(\omega)$, more corresponding to what here can be found as $-iT_{aq}(\omega)/\omega$. In [100] the authors underline how the weighting matrix is useful to better control the excitations and that when $V_{af}(\omega)$ is of full rank (i.e. $rank(V_{af}(\omega)) = min(N_a, N_f)$) the weighted pseudo-inverse coincides with the Moore-Penrose inverse, the pseudo inverse in Eq. (9), potentially refined by SVD in weak data handling. In [101] the *Coherence functions* were also used to select the best set of output locations in pseudo-inverse problems, while here the topology is well known and the whole dataset is proficiently used, the *Coherence functions* having not shown disrupting deficiencies at specific frequencies. Furthermore, not using any modal model identification, but only raw FRFs, no identification errors are cumulated, contrary to the dangers coming from a simplified/truncated model as highlighted in [102].

Table 2
Arrangement of the results in the direct vibro-acoustic analyses.

Section	Quantity	Structural excitation	Acoustic domain	Frequency domain	Figures
3.2	$V_{af}(\omega)$	S1, –	single dof [1974]	[20-1024] Hz	Fig. 4
3.2	$\mathbf{V}_{af}(\omega)$	S1, –	whole mesh	127.5 Hz	Fig. 5
3.2	$\mathbf{V}_{af}(\omega)$	S1, –	whole mesh	525.5 Hz	Fig. 6
3.2	$\mathbf{V}_{af}(\omega)$	S1, –	whole mesh	879.5 Hz	Fig. 7
3.3	$p(\mathbf{a}_a,\omega)$	S1, *blue noise-std*	single dof [1974]	[20-1024] Hz	Fig. 8
3.3	$p(\mathbf{a}_a,\omega)$	S1, *pink noise-sp*	single dof [1974]	[20-1024] Hz	Fig. 9
3.3	$p(\mathbf{a}_a,\omega)$	S1, *red noise-ra*	single dof [1974]	[20-1024] Hz	Fig. 10
3.3	$p(\mathbf{a}_a,\omega)$	S1, *violet noise-rap*	single dof [1974]	[20-1024] Hz	Fig. 11
3.4	$\mathbf{p}(\mathbf{a}_a,\omega)$	S1, *blue noise-std*	whole mesh	127.5 Hz	Fig. 12
3.4	$\mathbf{p}(\mathbf{a}_a,\omega)$	S1, *pink noise-sp*	whole mesh	525.5 Hz	Fig. 13
3.4	$\mathbf{p}(\mathbf{a}_a,\omega)$	S1, *red noise-ra*	whole mesh	127.5 Hz	Fig. 14
3.4	$\mathbf{p}(\mathbf{a}_a,\omega)$	S1, *violet noise-rap*	whole mesh	525.5 Hz	Fig. 15

a raw DIC-based dataset; on the same bottom line, but on the right side, are reported the active (yellow) and mute (dark grey) shakers.

In all the following 3D $\mathbb{C}$ maps, to obtain a precise *phase* comparison, the same projecting angle is kept among the tiles. A range scale in grey tones, on the left side, linearly maps the extremes of the function in the range. The minimal values (with sign) are rendered by darker tones, while maximal values by full brightness. On the range scale, with a short magenta line, the level of the function in the acoustic dof of inquiry is annotated; the same value is numerically added within the red text. The highlighted magenta dof ($a = 1974$) on the acoustic mesh – highlighted also by the magenta text – is used to extract the 2D graphs of vibro-acoustic functions. The *ebffr* are positioned in front and coloured in red tones, with the same colour scheme, but without any highlighted value or scale. A dark yellow dot (and text label) locates, on the structural maps of the *ebffr*, the active shaker; instead, a dark grey dot (and text label) is for the mute shaker; in the text of all the figures, due to this DIC-based dataset, shaker 1 is in structural dof $f = 10414$ in dark yellow, shaker 2 in structural dof $f = 4034$ in dark grey.

3.1. Brief notes about the simulations in the acoustic domain

In the literature of a recent past, e.g. see [1–8], the experiment-based vibro-acoustic problem was usually treated with coarse grids in both domains, at the time based on more traditional transducers, like sparse accelerometers and few microphones. Their limited dof number may prevent the appreciation of the contributions of specific local structural patterns in the blending of acoustic diffusion. But, with the advent of higher resolution instruments, it can also mask some noise patterns,

or also unwanted experimental errors, in the *ebffr*, which is diffused into the acoustic simulations, with unrealistic effects [79]. On the other side, *native* full-field techniques, like ESPI and DIC, have much cleaner *ebffr* fields with enhanced spatial resolution – *very dense* for ESPI and *high* for DIC – for a greater reliability of the experiment-based derivative calculations (especially as strains in [70]) and also of vibro-acoustic simulations, as it is pursued here, without the use of any field data interpolation to raise the spatial detail. To clearly show the potential of the *native* high spatial resolution of DIC-based datasets, a squared acoustic mesh was generated, of size 0.5 m × 0.5 m, with 101×101 dofs ($N_a = 10201$, 5 mm of acoustic grid spacing), centred on the vibrating plate and located 0.2 m above it. Note that any other acoustic mesh can be generated, in the limits of this simplified approach, of the computational costs and especially of memory allocation. As it is noted later, the acoustic mesh shows simpler patterns than those on the structural domain, due to the longer wavelength in the air diffusion. However, these simulations try to show the reliability of the procedure also in spatially hyper-detailed domains, in view of airborne strain mapping. Furthermore, newer high-speed cameras have much higher fps, therefore close to human speech or mid frequencies: this wants to be a proof of a DIC-based procedure, better described in Section 3.6, to be exploited also with the modern advances of electronics for more complex patterns in broader frequency ranges. In this exemplification, the air parameters were idealised in $c_0 = 300.0$ m/s and $\rho_0 = 1.204$ kg/m^3, reminding how specific attentions to other air conditions should be paid, such as humidity, temperature and altitude, related to the parts' testing and applications.
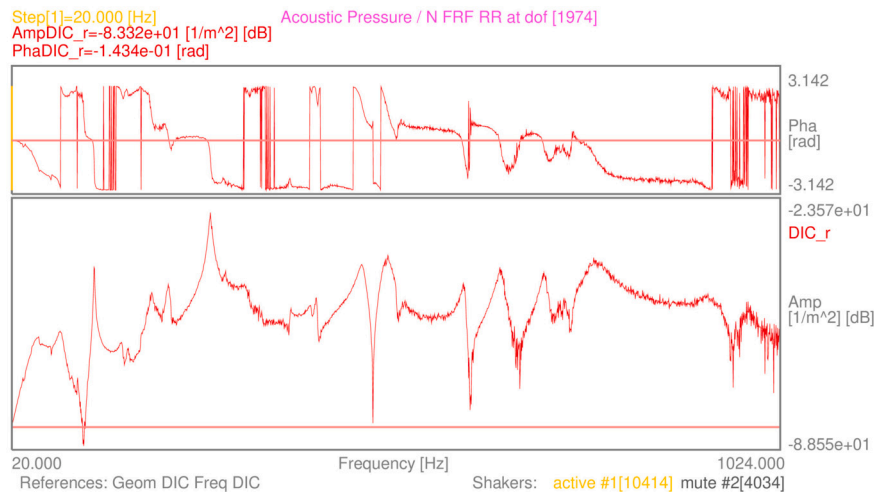

Fig. 4. Example of *vibro-acoustic FRF* $V_{af}(\omega)$ in the $\mathbb{C}$ spectrum graph, evaluated in acoustic dof $a = 1974$ with excitation from shaker 1 (structural dof $f = 10414$).
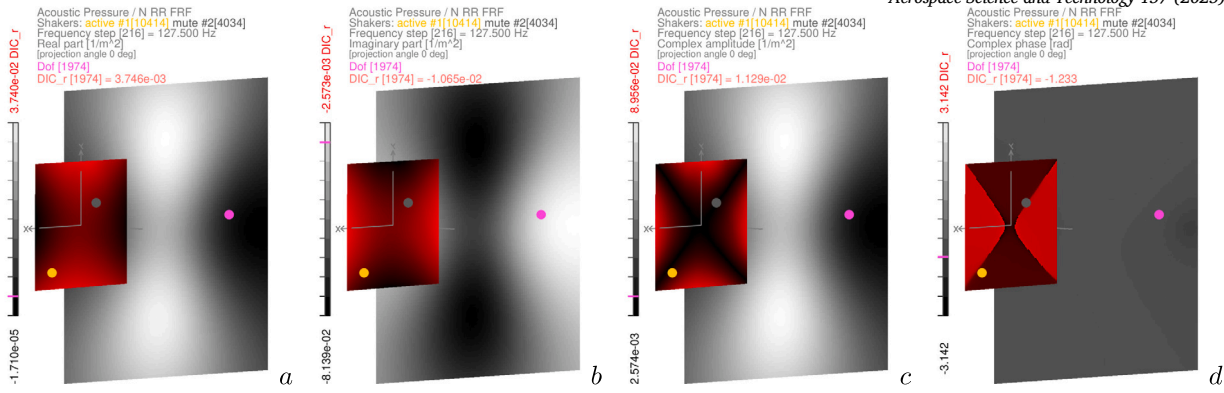
Fig. 5. Examples of $V_{af}(\omega)$ field in grey tones, with corresponding *ebffr* in red tones, evaluated at the specific frequency of 127.5 Hz, highlighted (magenta) acoustic dof $a = 1974$, excitation from shaker 1, in its $\mathbb{C}$ parts: *real part* in *a*, *imaginary part* in *b*, *complex amplitude* in *c* and *complex phase* in *d*.
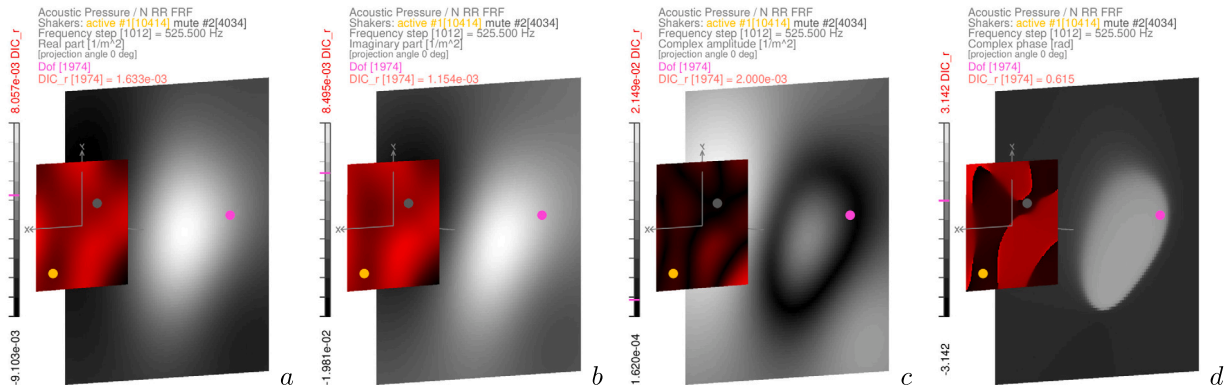

Fig. 6. Examples of $V_{af}(\omega)$ field in grey tones, with corresponding *ebffr* in red tones, evaluated at the specific frequency of 525.5 Hz, highlighted (magenta) acoustic dof $a = 1974$, excitation from shaker 1, in its $\mathbb{C}$ parts: *real part* in *a*, *imaginary part* in *b*, *complex amplitude* in *c* and *complex phase* in *d*.
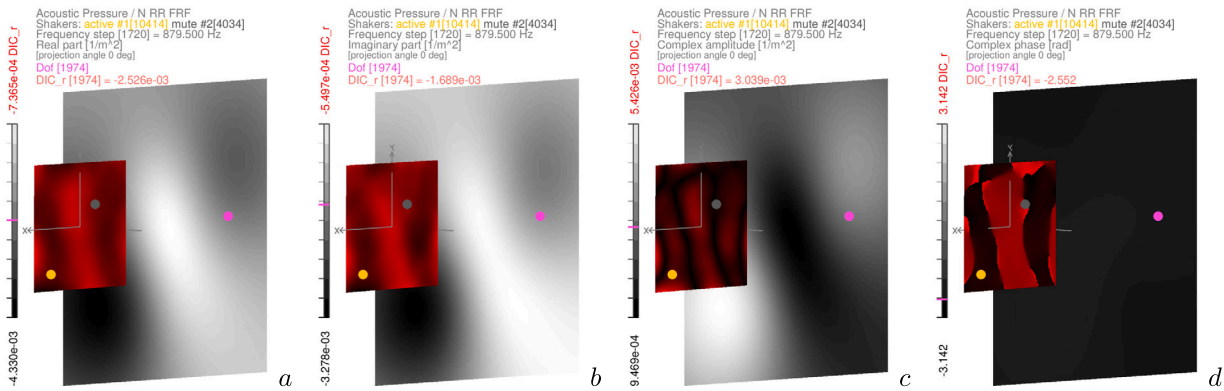

Fig. 7. Examples of $V_{af}(\omega)$ field in grey tones, with corresponding *ebffr* in red tones, evaluated at the specific frequency of 879.5 Hz, highlighted (magenta) acoustic dof $a = 1974$, excitation from shaker 1, in its $\mathbb{C}$ parts: *real part* in *a*, *imaginary part* in *b*, *complex amplitude* in *c* and *complex phase* in *d*.

3.2. Evaluation of the vibro-acoustic transfer matrix

The evaluation of $V_{af}(\omega)$ is shown directly from the *ebffr*, as formulated in Section 2.2. No structural FEM was needed, whereas great detail and field quality were assured by accurate DIC-based full-field optical measurements, nowadays obtainable with more ease, as explained in Section 2.1. Note how the *vibro-acoustic transfer matrix* preserves, thanks to the $\mathbb{C}$ *nature* of the *ebffr*, all the real-life conditions of the test: no simplifications were made in the damping distribution, nor in the materials' properties, nor in the boundary conditions, nor in the identification of any modal base (or truncation of).

In Fig. 4 a single example, extracted from $V_{af}(\omega)$, is reported: it is the vibro-acoustic FRF from shaker 1 (located at structural dof $f = 10414$)

and acoustic dof $a = 1974$. The data retain completely the $\mathbb{C}$ nature of the *ebffr*, especially in the damping around resonances and anti-resonances, or in the blending at any other frequency. Note that these results are hardly obtainable by synthetic structural models without a complete tuning or model updating [44–46], a general damping modelling and a high-order $\mathbb{C}$ modal base, to really minimise the FRF synthesis errors.

In Figs. 5, 6 and 7 the data of $V_{af}(\omega)$ are displayed in the whole acoustic mesh as grey tones, behind the evaluated $H_{d_nqf}(\omega)$ of the vibrating plate in red tones, at 127.5 Hz, at 525.5 Hz and at 879.5 Hz respectively, with all the components of both the structural and acoustic domains. The levels of $V_{af}(\omega)$ can hint to how the components are blended or scaled into the whole data representation, once a specific excitation is later used to evaluate $p(a_a, \omega)$ in Eq. (7) and Section 3.4.
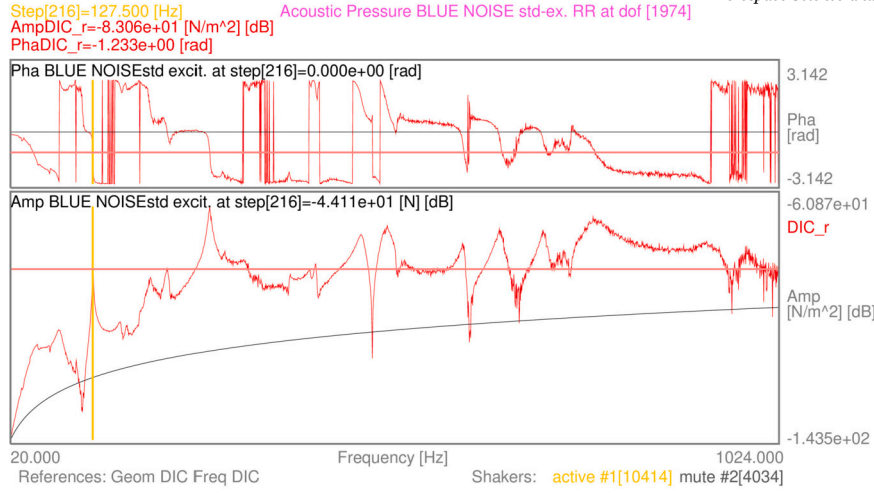
Fig. 8. Example of $p(\boldsymbol{a}_a, \omega)$ (in red) in the $\mathbb{C}$ spectrum graph, evaluated in acoustic dof $a = 1974$, from a *blue noise-std* excitation (in black) in shaker 1.

The evaluations of $\boldsymbol{V}_{af}(\omega)$ are shown over the whole acoustic field, maintaining all the relations and phase delays inside $\boldsymbol{H}_{d_n qf}(\omega)$, further fused in the summation by Green's functions of Eq. (3). The distance of the acoustic mesh from the plate is a true variable of the blending, or fusion with fading effects, of each contribution from specific areas on the vibrating structure: this reveals the proximity to specific nodal lines of the *ebffr*, in particular at lower frequencies. In Fig. 5c the *complex amplitude* of $\boldsymbol{V}_{af}(\omega)$ mimics the *receptance* shape (in front), whose pattern is quite simple at 127.5 Hz, but the agreement seems higher with the *real part* in Fig. 5a or with the *imaginary part* of Fig. 5b; instead, the *complex phase* of $\boldsymbol{V}_{af}(\omega)$ in Fig. 5d appears quite uniform due to the norm in Green's function, while the *ebffr* shows a clearly uneven shape. In Figs. 6a, b the *real* and *imaginary parts* of $\boldsymbol{V}_{af}(\omega)$ at 525.5 Hz start to show how the structural complexity in the *ebffr*, mixed by $\boldsymbol{T}_{aq}(\omega)$ in Eq. (6), fades when the acoustic mesh has a greater distance, from the vibrating plate, than that of the *near-field* [1,2,85]. Figures 6c, d show indeed the blending mediated by $\boldsymbol{T}_{aq}(\omega)$, with quite different *complex amplitude* and *phase* patterns of $\boldsymbol{V}_{af}(\omega)$ from the *ebffr*: nodal lines appear, as could not be easily predicted by just looking at a single *real* or *imaginary part*. The amplitude of the *ebffr* in the extreme corners also seems to have quite a relevance onto the far distance behaviour of $\boldsymbol{V}_{af}(\omega)$. Note that the *complex phase* has smoothed transitions on the acoustic mesh, revealing the nature of a field of travelling waves. Instead, as was shown in [79], at closer distances the *ebffr* project into $\boldsymbol{V}_{af}(\omega)$ mesh with a much clearer reproduction of nodal lines' ar-

rangement. This is even more manifest in Figs. 7a, b, where the *real and imaginary parts* on the acoustic mesh mix, in a smoother field, those structural components with a more articulated pattern. In the *complex phase* of Fig. 7d, the many discontinuities in the *ebffr* are evened in a nearly constant field for $\boldsymbol{V}_{af}(\omega)$. With the rise of frequencies, the *receptance* maps exhibit an increased complexity in the shape, as can be noted in Fig. 6c at 525.5 Hz, and even more in Fig. 7c at 879.5 Hz; instead, the evaluated blending in every acoustic dof ($N_a = 10201$) of $\boldsymbol{V}_{af}(\omega)$ field, due to all the contributions across S, has quite a different shape now, coming from the summation of $N_q = 11988$ Green's function contributions, properly phased in Eqs.(4)-(6), which contain therefore the distance vector norm evaluation of Eq. (3).

3.3. Evaluation of acoustic pressure spectra from structural excitations

The full retention of the rich $\mathbb{C}$ nature of $\boldsymbol{V}_{af}(\omega)$ – with unsimplified $\mathbb{C}$ parts, nor modal model truncation, nor identification errors in the whole frequency range – is emphasised once the signatures of the excitations are adopted, e.g., as modelled in Section 2.3, for the deployment of the acoustic pressure $p(\boldsymbol{a}_a, \omega)$ in the whole frequency domain analysed. Four $F(\omega)$ signals were simulated here in shaker 1: *blue noise-std* (Eq. (11), $\alpha = -1$), *pink noise-sp* (Eq. (12), $\alpha = 1$), *red noise-ra* (Eq. (13), $\alpha = 2$), and *violet noise-rap* (Eq. (14), $\alpha = -2$).

Compared to the shape of $V_{af}(\omega)$ shown in Fig. 4, in Fig. 8 the *blue noise-std* excitation (in black) introduces only a *complex amplitude* scal-
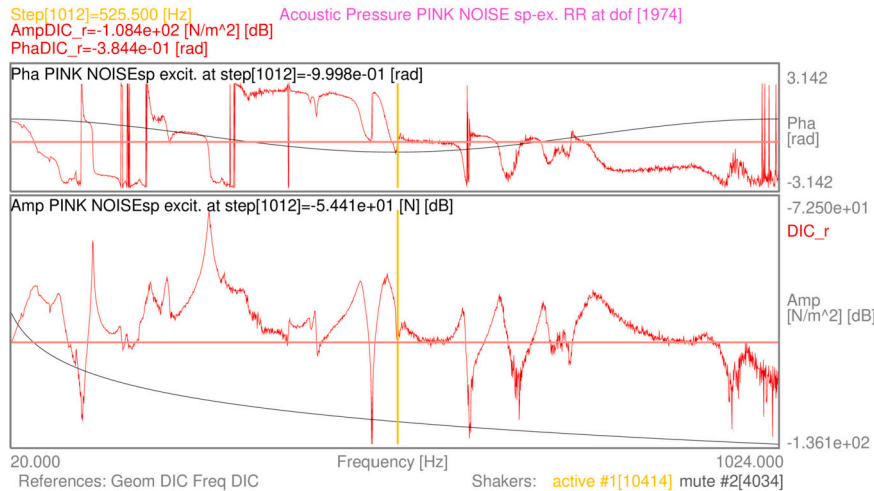

Fig. 9. Example of $p(\boldsymbol{a}_a, \omega)$ (in red) in the $\mathbb{C}$ spectrum graph, evaluated in acoustic dof $a = 1974$, from a *pink noise-sp* excitation (in black) in shaker 1.

Fig. 10. Example of $p(\boldsymbol{a}_a, \omega)$ (in red) in the $\mathbb{C}$ spectrum graph, evaluated in acoustic dof $a = 1974$, from a *red noise-ra* excitation (in black) in shaker 1.
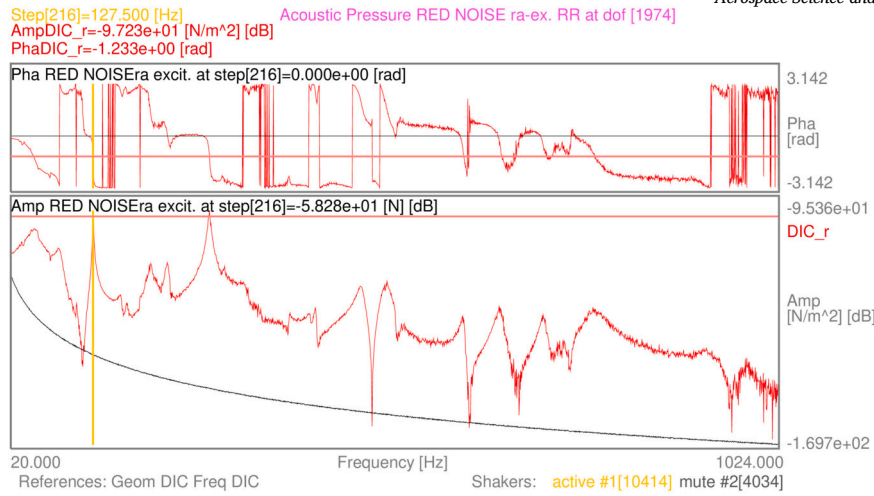
ing in the spectrum of $p(\boldsymbol{a}_a, \omega)$ (in red) at dof $a = 1974$, as function of the frequency-dependent amplitude, without any *phase* modification. Specifically, the *complex amplitude* of $p(\boldsymbol{a}_a, \omega)$ sees a moderate raising of the higher frequency components due to the *blue noise* nature.

In Fig. 9, instead, again comparing it to the shape of $V_{af}(\omega)$ shown in Fig. 4, the *pink noise-sp* excitation introduces now a combined *complex amplitude* scaling in the spectrum of $p(\boldsymbol{a}_a, \omega)$ at dof $a = 1974$, as function of the frequency-dependent amplitude, together with the sinusoidal *phase* modification. Specifically, the *complex amplitude* of $p(\boldsymbol{a}_a, \omega)$ sees a moderate drop of the higher frequency components due to the *pink noise* nature, while the *complex phase* of $p(\boldsymbol{a}_a, \omega)$ sees the additional contribution of the sinusoidal phase in the excitation, coming to a completely different spectrum.

Once the excitation signature is formulated with added randomness in the amplitudes as for *red noise-ra*, the *complex amplitudes* of $p(\boldsymbol{a}_a, \omega)$ in Fig. 10 see a marked drop of the higher frequency component. The added randomness is only a scattering of $\pm 2.5\%$ of the *red noise* curve, therefore appearing as a limited increase in thickness of the amplitude uncertainties in both black and red functions. The *phase* has no modifications compared to that shown in Fig. 4 for $V_{af}(\omega)$, the excitation being as a $\mathbb{R}$ signal.

The *violet noise-rap* excitation introduces in Fig. 11 a *complex amplitude* scaling in the spectrum of $p(\boldsymbol{a}_a, \omega)$, compared to the shape of $V_{af}(\omega)$ shown in Fig. 4, as function of the frequency-dependent amplitude, and

specific sinusoidal *phase* modifications, leading to quite a different shape of the functions. On top of those modifications, a limited randomness is given on both the *complex amplitude* (scattering of $\pm 2.5\%$) and *complex phase* (scattering of $\pm 7.5\%/\pi$ rad against Fig. 9). Contrary to Fig. 10, the *complex amplitude* of $p(\boldsymbol{a}_a, \omega)$ sees a marked raising of the higher frequency components due to the *violet noise* nature.

Furthermore, by varying the parameters in the $\mathbb{C}$ coloured noise with randomness in both the amplitude and phase, as that of Eq. (14), it is possible to appreciate how the whole *experiment-based full-field approach* is ready to be fed by real-life spectra, those obtained by the estimation of actual forces on prototypes or assembled components, without any specific approximation, but retaining the rich dynamics of the *ebffr*.

3.4. Evaluation of acoustic pressure fields from structural excitations

The $p(\boldsymbol{a}_a, \omega)$ fields are here shown in the whole acoustic mesh, or spatial domain; instead, in Section 3.3 the spectra were shown in the entire retained frequency domain, but in only the single magenta dof $a = 1974$. As in Section 3.2 for $V_{af}(\omega)$, at specific frequencies of interest, $p(\boldsymbol{a}_a, \omega)$ fields are here shown in all their $\mathbb{C}$ components. The excitation signals are the same 4 $F(\omega)$ simulated in Section 3.3.

The $p(\boldsymbol{a}_a, \omega)$ field in Fig. 12 shows how $V_{af}(\omega)$ of Fig. 5 is influenced by the *blue noise-std* excitation. Indeed, as witnessed by the punctual values in the magenta dof $a = 1974$, only a $\mathbb{R}$ amplitude scaling is applied,
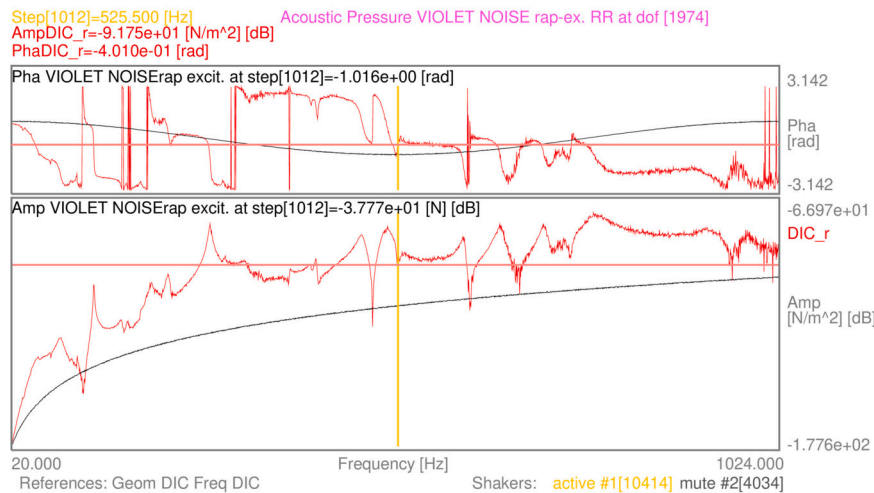

Fig. 11. Example of $p(\boldsymbol{a}_a, \omega)$ (in red) in the $\mathbb{C}$ spectrum graph, evaluated in acoustic dof $a = 1974$, from a *violet noise-rap* excitation (in black) in shaker 1.
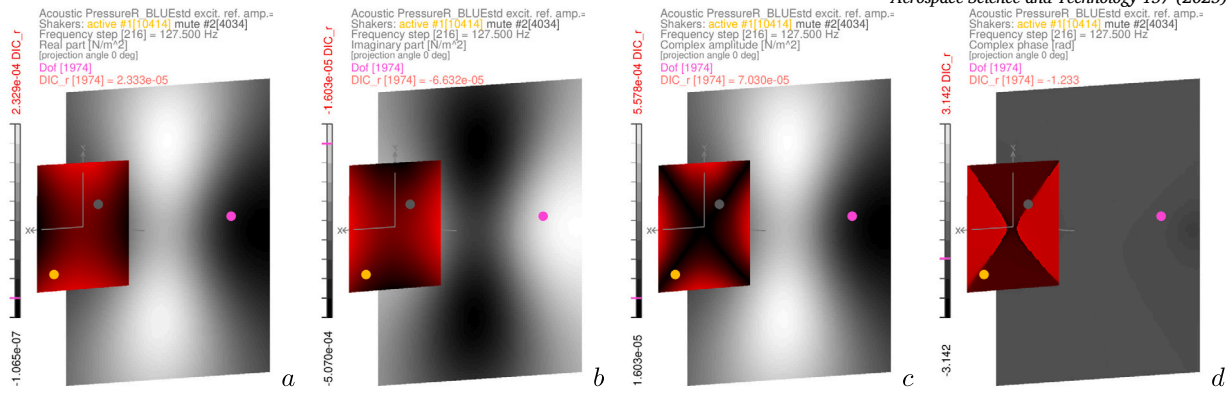
Fig. 12. Examples of $p(a_a, \omega)$ field in grey tones, with corresponding *ebffr* in red tones, evaluated at the specific frequency of 127.5 Hz, highlighted (magenta) acoustic dof $a = 1974$, *blue noise-std* excitation from shaker 1, in its $\mathbb{C}$ parts: *real part* in a, *imaginary part* in b, *complex amplitude* in c and *complex phase* in d.
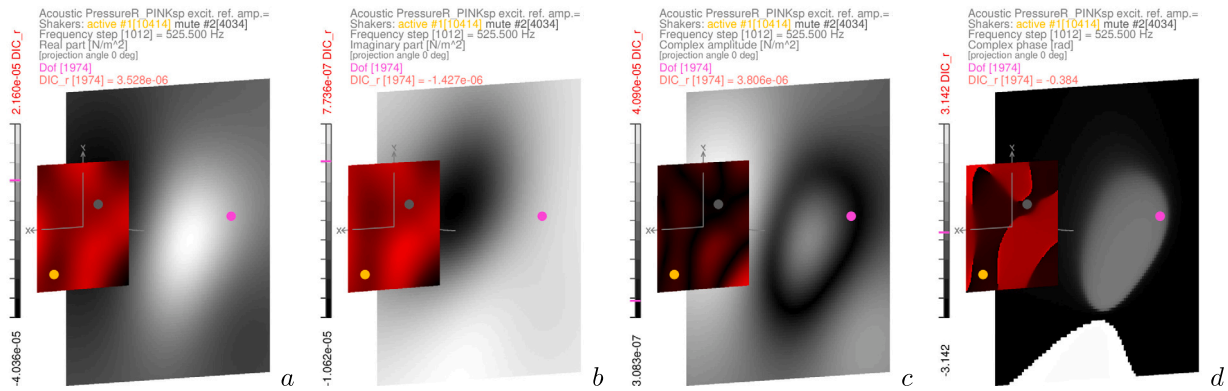

Fig. 13. Examples of $p(a_a, \omega)$ field in grey tones, with corresponding *ebffr* in red tones, evaluated at the specific frequency of 525.5 Hz, highlighted (magenta) acoustic dof $a = 1974$, *pink noise-sp* excitation from shaker 1, in its $\mathbb{C}$ parts: *real part* in a, *imaginary part* in b, *complex amplitude* in c and *complex phase* in d.

without any phase variation, therefore the maps in both figures 5 and 12 have the same relative mapping and tones, albeit of different quantities ($V_{af}(\omega)$ vs $p(a_a, \omega)$), while the *ebffr* remain the same.

The use of a *pink noise-sp* excitation brings the $p(a_a, \omega)$ maps of Fig. 13 to be compared against $V_{af}(\omega)$ of Fig. 6. Now the $\mathbb{C}$ nature of $F(\omega)$ interacts with a multiplication of $V_{af}(\omega)$ data parts. A change in the relative mapping happens in the *imaginary part* and in the *complex phase*. The *imaginary part* changes the sign in Fig. 13b, and therefore the grey tones as a negative image of Fig. 6b. The *complex phase* in Fig. 13d drops – the whole map is shifted down in the range – by ~1 rad compared to that in Fig. 6d, but being wrapped in the range $[-\pi, \pi]$ rad, it is represented in bright tones of grey instead of darkest greys, as it

appears in Fig. 13d, restarting at the top of the range. Also, the relative mapping of the *complex phase* is not touched. This scaling does not touch either the relative mapping of the *real part* or the *complex amplitude*, therefore the pairs of Figs. 6a, 13a and Figs. 6c, 13c appear with the same relative mapping and tones.

With the addition of an amplitude randomness in the *red noise-ra* $F(\omega)$, the $p(a_a, \omega)$ field in Fig. 14 is again obtained as a $\mathbb{R}$ scaling of $V_{af}(\omega)$ of Fig. 5, therefore without any relative mapping changes, as also commented for the effect of the *blue noise-std* excitation in Fig. 12.

Instead, in Fig. 15 the randomness in the *complex amplitude* and *phase* of $F(\omega)$, modelled as *violet noise-rap* signal, brings a new $\mathbb{C}$ scaling of $V_{af}(\omega)$ in Fig. 6. While the same approach followed in the discussion
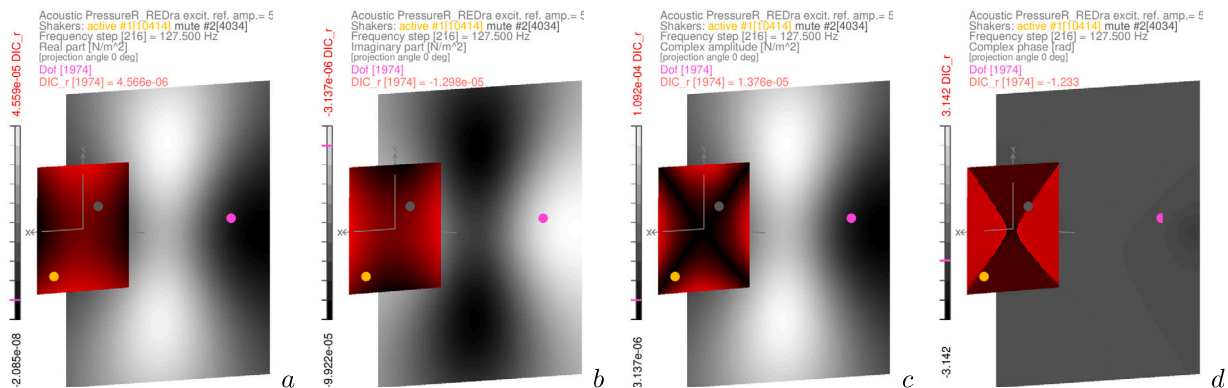

Fig. 14. Examples of $p(a_a, \omega)$ field in grey tones, with corresponding *ebffr* in red tones, evaluated at the specific frequency of 127.5 Hz, highlighted (magenta) acoustic dof $a = 1974$, *red noise-ra* excitation from shaker 1, in its $\mathbb{C}$ parts: *real part* in a, *imaginary part* in b, *complex amplitude* in c and *complex phase* in d.
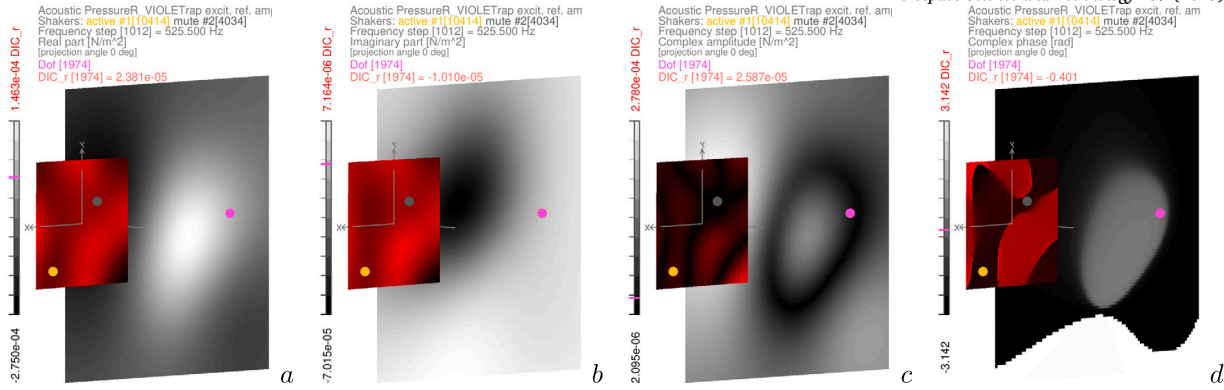
Fig. 15. Examples of $p(a_a, \omega)$ field in grey tones, with corresponding *ebffr* in red tones, evaluated at the specific frequency of 525.5 Hz, highlighted (magenta) acoustic dof $a = 1974$, *violet noise-rap* excitation from shaker 1, in its $\mathbb{C}$ parts: *real part* in a, *imaginary part* in b, *complex amplitude* in c and *complex phase* in d.

Table 3
Arrangement of the results in the pseudo-inverse vibro-acoustic analyses.

| Section	Quantity	Acoustic domain, excitation	Structural domain	Frequency domain	Figures
3.5	$V_{fa}^+(\omega)$	single dof [1974], –	S1	[20-1024] Hz	Fig. 16
3.6	$\hat{F}_{S1}(\omega)$	whole mesh, *blue noise-std*	S1	[20-1024] Hz	Fig. 17
3.6	$Err_{F_{S1}}(\omega)$	whole mesh, *blue noise-std*	S1	[20-1024] Hz	Fig. 18
3.6	$\hat{F}_{S1}(\omega)$	whole mesh, *pink noise-sp*	S1	[20-1024] Hz	Fig. 19
3.6	$Err_{F_{S1}}(\omega)$	whole mesh, *pink noise-sp*	S1	[20-1024] Hz	Fig. 20
3.6	$\hat{F}_{S1}(\omega)$	whole mesh, *red noise-ra*	S1	[20-1024] Hz	Fig. 21
3.6	$Err_{F_{S1}}(\omega)$	whole mesh, *red noise-ra*	S1	[20-1024] Hz	Fig. 22
3.6	$\hat{F}_{S1}(\omega)$	whole mesh, *violet noise-rap*	S1	[20-1024] Hz	Fig. 23
3.6	$Err_{F_{S1}}(\omega)$	whole mesh, *violet noise-rap*	S1	[20-1024] Hz	Fig. 24
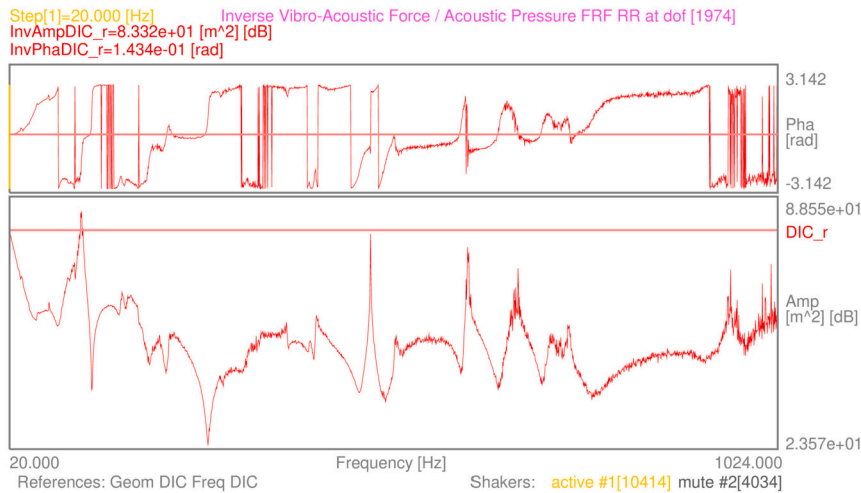
Fig. 16. Example of *pseudo-inverse vibro-acoustic FRF* $V_{fa}^+(\omega)$ in the $\mathbb{C}$ spectrum graph, evaluated as force in shaker 1 (structural dof $f = 10414$) over the airborne acoustic pressure from dof $a = 1974$.

about Fig. 13 could be recalled, here in Fig. 15 the randomness adds a different $\mathbb{C}$ scaling factor, therefore the $p(a_a, \omega)$ maps have slight changes, with different shifts, but particularly manifest among only the relative mapping of the *complex phases* of Figs. 13d, 15d against Fig. 6d. But it is the relative mapping difference, between Fig. 13d and Fig. 15d, which suggests that also the other *complex parts* receive a newly shaped $\mathbb{C}$ amplification factor. The shape of the wrapped *phase* witnesses a different blending of the *real* and *imaginary parts* in Figs. 15a, b, therefore also in the *complex amplitude* of Fig. 15c, even if not easily detectable without proper numerical tools such as MAC and FRAC maps, as widely used instead in [70,79], to compare the results in the same spatial field, but here of useless complexity.

3.5. Evaluation of the pseudo-inverse airborne vibro-acoustic FRFs

Implementing Eq. (9) with $N_f = 1$, the *pseudo-inverse vibro-acoustic FRFs* $V_{fa}^+(\omega)$ (or *acoustic-vibrational FRFs* of *force* over airborne *sound pressures*) can be evaluated, as sketched in the single $V_{fa}^+(\omega)$ of Fig. 16, where the acting acoustic dof is $a = 1974$ from the airborne pressure field, and the force is retrieved in the structural dof $f = 10414$ of shaker 1. The same can be repeated for all the $N_a = 10201$ acoustic dofs in the mesh, here retained from the *direct vibro-acoustic* simulations. However, as suggested in Section 3.8, the mesh might be defined also by procedure's tuning tests with microphone shifting arrays, when therefore new $V_{fa}^+(\omega)$ should be evaluated accordingly. The comparison between
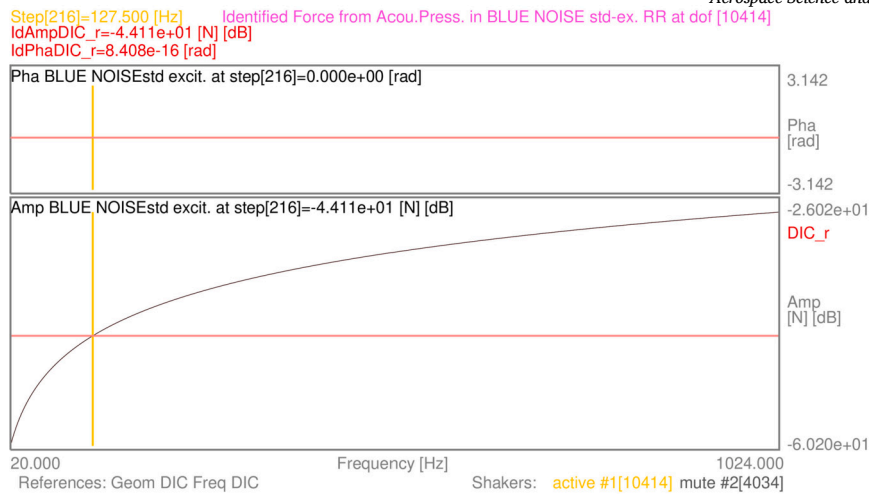
Fig. 17. Example of *identified force* $\hat{F}_{S1}(\omega)$ (in red) in the spectrum graph, evaluated against the *blue noise-std* force (in black) in shaker 1, which originated the whole airborne acoustic pressure field.
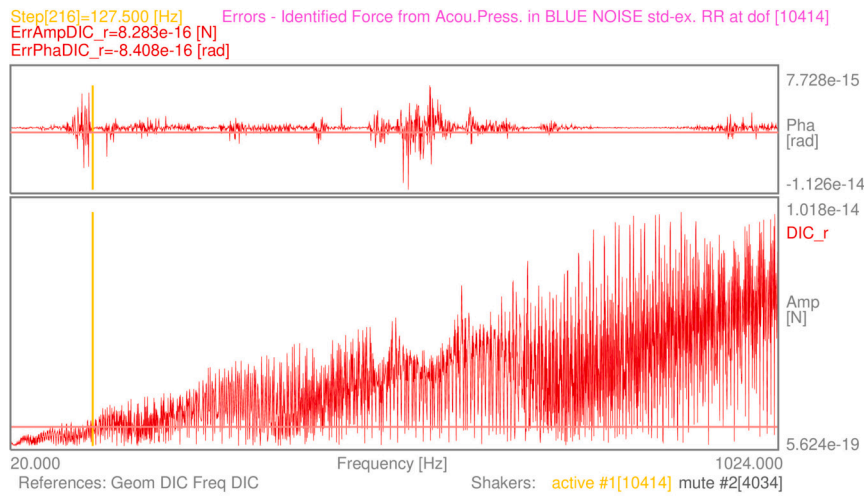

Fig. 18. Errors $Err_{F_{S1}}(\omega)$ of the *identified force* $\hat{F}_{S1}(\omega)$ in the spectrum graph, while a *blue noise-std* force in shaker 1 was the origin of the whole airborne acoustic pressure field.

$V_{af}(\omega)$ of Fig. 4 and $V_{fa}^{+}(\omega)$ of Fig. 16 is straightforward, with a clear reflection of the whole data without noticeable distortions. Note how the whole $\mathbb{C}$ information is fully retained in the pseudo-inversion, up to the numerical precision of the routines. The successful evaluation of $V_{fa}^{+}(\omega)$ plays therefore a crucial role in the following force identifications from airborne $\hat{p}(a_a, \omega)$ fields.

3.6. Assessing the retrieval of the force induced by airborne acoustic pressure fields

For the evaluation of the force $\hat{F}_{S1}(\omega)$, where $S1$ means structural dof $f = 10414$ of shaker 1, by means of Eq. (8), the whole airborne $\hat{p}(a_a, \omega)$ field acting on the N_a dofs of the acoustic mesh was used, together with the corresponding $V_{fa}^{+}(\omega)$ in Section 3.5. To assess the quality of the identification process, the airborne $\hat{p}(a_a, \omega)$ were exactly taken from all the $p(a_a, \omega)$ fields, previously generated by means of the same coloured noises in Section 2.3 and 3.3, without adding any extra noise: $\hat{p}(a_a, \omega) \equiv p(a_a, \omega)$. This checks the right handling of the $\mathbb{C}$ datasets in all the modelled scenarios of the 4 excitations.

In Fig. 17 the original *blue noise-std* excitation $F(\omega)$, with the amplitude that grows with ω and no phase lags, and the identified force $\hat{F}_{S1}(\omega)$ are shown together, completely superimposed, amplitude and phase extremes being coded in the same manner, with only 3 deci-

mals. Only Eq. (10) in Fig. 18 can show the differences in such a small range: $Err_{F_{S1}}(\omega)$ lies in the *complex amplitude* range of $[5.624e{-}19, 1.018e{-}14]$ [N], against a corresponding linear *complex amplitude* range for $\hat{F}_{S1}(\omega)$ and $F(\omega)$ of $[4.886e{-}05, 5.000e{-}02]$ [N]; for the *complex phase*, $Err_{F_{S1}}(\omega)$ is in the range $[-1.126e{-}14, 7.728e{-}15]$ [rad], against a null phase shown by $\hat{F}_{S1}(\omega)$ and $F(\omega)$.

In Fig. 19 the *pink noise-sp* $F(\omega)$ and $\hat{F}_{S1}(\omega)$ are shown together, again totally superimposed, with frequency-decreasing amplitude and sinusoidal phase lag. In this case, $Err_{F_{S1}}(\omega)$ in Fig. 20 has the *complex amplitude* in the range $[3.610e{-}18, 8.696e{-}15]$[N], against a corresponding linear amplitude range for $\hat{F}_{S1}(\omega)$ and $F(\omega)$ of $[4.886e{-}05, 5.000e{-}02]$ [N] in Fig. 19; the *complex phase* of $Err_{F_{S1}}(\omega)$ is in the range $[-2.134e{-}13, 1.913e{-}13]$ [rad], against a range of $[-1, 1]$ [rad] for $\hat{F}_{S1}(\omega)$ and $F(\omega)$.

In Fig. 21 the *red noise-ra* $F(\omega)$ – with remarkable frequency-decreasing amplitude but zero phase lag – and $\hat{F}_{S1}(\omega)$ are shown together, again totally superimposed, although randomness is present in the functions' amplitude. Also in this case, only from Eq. (10) – shown in Fig. 22 – can the information about the differences be drawn: $Err_{F_{S1}}(\omega)$ has the *complex amplitude* in the range $[3.391e{-}20, 8.486e{-}15]$ [N], against a corresponding linear amplitude range of $[9.495e{-}07, 5.087e{-}02]$ [N] for $\hat{F}_{S1}(\omega)$ and $F(\omega)$. Note the effect of randomness on the amplitude, which exceeds the 0.05 N of F_0. Against

the null phase represented by $\hat{F}_{S1}(\omega)$ and $F(\omega)$, the *complex phase* differences of $Err_{F_{S1}}(\omega)$ are in the range $[-8.112e{-}15, 1.544e{-}14]$ [rad].

The case of Fig. 23 shows the *violet noise-rap* $F(\omega)$, with remarkable frequency-increasing amplitude and sinusoidal phase lag, and $\hat{F}_1(\omega)$ totally superimposed, although randomness is present in the functions' *complex amplitude* and *phase*. Also in this last case, only from Fig. 24 can the differences be drawn: $Err_{F_{S1}}(\omega)$ has the *complex amplitude* in the range $[9.180e{-}19, 9.465e{-}15]$ [N], against a corresponding linear amplitude range of $[1.942e{-}05, 5.105e{-}02]$ [N] for $\hat{F}_{S1}(\omega)$ and $F(\omega)$, with the effect of randomness on the amplitude, exceeding F_0. The *complex phase* of $\hat{F}_{S1}(\omega)$ and $F(\omega)$, affected by randomness, lies in the range of $[-1.024, 1.024]$ [rad], whereas that of $Err_{F_{S1}}(\omega)$ is in the range of $[-1.977e{-}13, 1.998e{-}13]$ [rad].

The scattering of the errors might seem wider if taken only from absolute values of the extremes. Once instead the errors are normalised against the *complex amplitudes* and *phases* of the functions, as in the last two columns of Table 4 and Table 5 respectively, the relative errors appear much more constrained in the same very limited range for all types of noises, despite the high resolution of both structural and acoustic domains. For the $\hat{F}_{S1}(\omega)$ *complex amplitudes* this relative error range has the widest extremes in $[1.151e{-}14, 2.036e{-}13]$ in Table 4,

for the identified *phases* it is in $[-1.931e{-}13, 1.951e{-}13]$, taking the sign of the phase in Table 5. Note that such accurate results, both in the *complex amplitudes* and *phases*, were obtained with the contributions of $N_q = 11988$ structural dofs and of $N_a = 10201$ acoustic dofs, with all the $\mathbb{C}$ multiplications and divisions involved in the force identification of Eq. (8). It appears that the number of dofs brings a slight penalty in the quality of the results: in [78], the amplitude relative errors were in the range $[1.402e{-}14, 2.207e{-}14]$ with *white noise-std* excitation, but in that case with a lower dof number ($N_q = 2907$, $N_a = 2601$), involving around 1/16 of the dataset size and relative maths. Furthermore, once $Err_{F_{S1}}(\omega)$ is divided by the amplitudes, it appears close to the 64 bit machine precision for `double` floatings (machine epsilon [103,104] of $2^{-52} \approx 2.220e{-}16$), used by the custom C-language computational engine, refining routines from [98] and OpenMP libraries.

The quality assessment of the airborne force retrieval can be crucial. It permits the further airborne structural dynamics' characterisation of the testing components, for enhanced studies about the dynamic distributions of displacements and strains/stresses. The latter, together with the tools from fatigue life predictions, will be fully deployed in further research about flexible components loaded by airborne pressure fields.
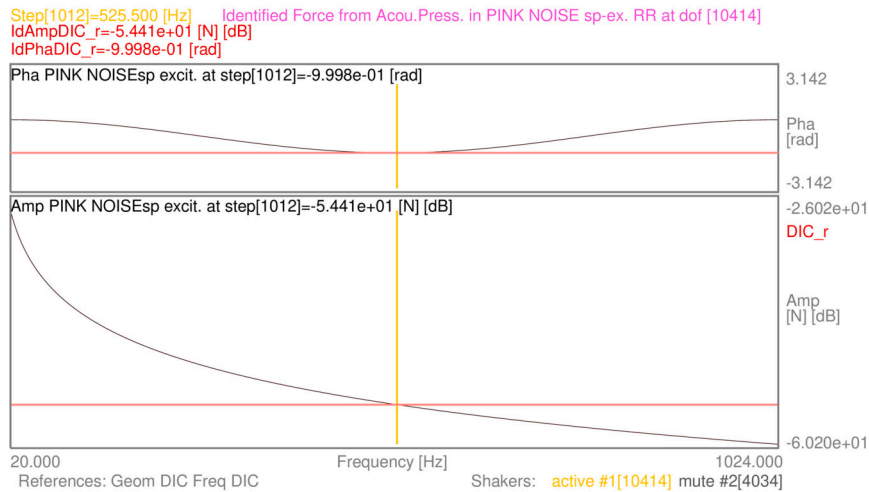

Fig. 19. Example of *identified force* $\hat{F}_{S1}(\omega)$ (in red) in the spectrum graph, evaluated against the *pink noise-sp* force (in black) in shaker 1, which originated the whole airborne acoustic pressure field.
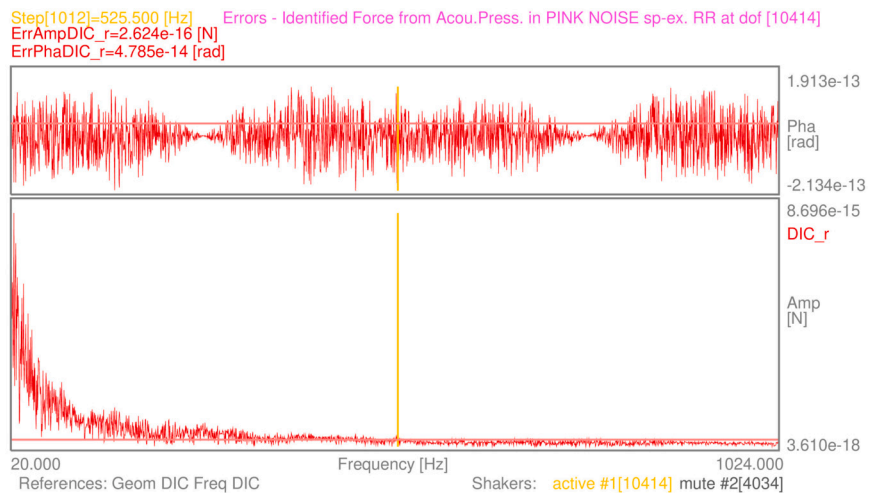

Fig. 20. Errors $Err_{F_{S1}}(\omega)$ of the *identified force* $\hat{F}_{S1}(\omega)$ in the spectrum graph, while a *pink noise-sp* force in shaker 1 was the origin of the whole airborne acoustic pressure field.
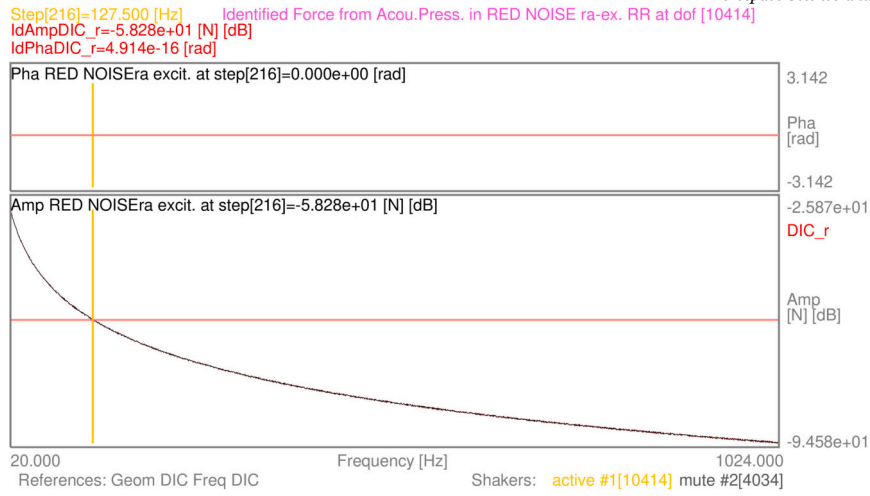
Fig. 21. Example of *identified force* $\hat{F}_{S1}(\omega)$ (in red) in the spectrum graph, evaluated against the *red noise-ra* force (in black) in shaker 1, which originated the whole airborne acoustic pressure field.
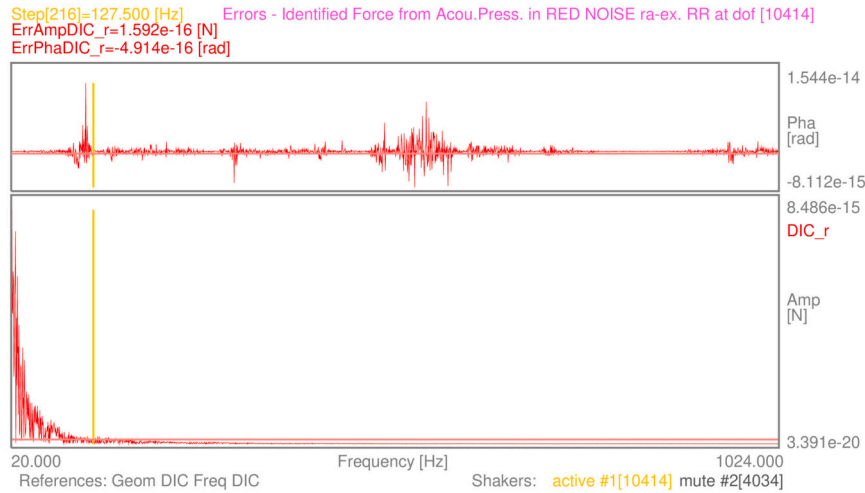

Fig. 22. Errors $Err_{F_{S1}}(\omega)$ of the *identified force* $\hat{F}_{S1}(\omega)$ in the spectrum graph, while a *red noise-ra* force in shaker 1 was the origin of the whole airborne acoustic pressure field.

3.7. Further discussion of the results

To summarise the methodological achievements in the examples of the above Sections, further global discussion is felt appropriate. It can also explain more clearly the reasons behind the proposed results and the message that is carried out by this research work. It can surely be advanced that DIC-based *ebffr* clearly confirmed in vibro-acoustics one of the conclusions made nearly 40 years ago in [5]: "*[..] the more complex the source is, the more accurate results can be obtained*".

Sections 3.2-3.4 have explored – by some examples among the thousand available – what is achievable in *direct vibro-acoustics* by means of accurate DIC-based high-resolution *full-field receptances* obtained from dynamic testing, in both spatial and frequency *complex-valued* domains. Unprecedented detail is shown for both the *vibro-acoustic transfer matrix* $V_{af}(\omega)$ and the *pressure fields* $p(a_a, \omega)$ from known excitation forces, which mimic real-life testing acquisitions as in Section 2.3, but without any FEM to build nor to tune, nor damping simplifications. Note also that most of FEM follows a $\mathbb{R}$ formulation, as remarked in Section 1, therefore unable to strictly represent real-life behaviour of structures at this detail and precision, even after extensive tuning. Furthermore, no EFFMA [46] was here applied, which means no truncation/identification/order errors were cumulated in the *ebffr* datasets. The latter carry

instead the acquisition errors in real testing, to be minimised as suggested in Section 2.1.

The quite simple formulation introduced in Section 2.2 – in the wake of Rayleigh integral approximation – proved to easily handle the high detail in both the structural and acoustic domains, thanks to the quality of DIC-based *ebffr*, the precise blending of the Green's functions and of the ubiquitous $\mathbb{C}$ formulation, without simplifications nor specific cutting projections. This clearly demonstrates that also DIC is becoming of interest in the experiment-based *direct vibro-acoustic* simulations, while in literature (e.g., in [63]) *native* optical full-field techniques usually dared not go beyond the more traditional structural dynamics (e.g., EFFMA or eigensystem realisation), neither assess such spatial detail in vibro-acoustics. Indeed, the low level of noise in the high-speed DIC-based *ebffr* dataset – here used – proved to work as a very good compromise among field resolution, frequency range and test execution time[14]. Furthermore, the stereo DIC-based datasets may come with 3D *receptances*, therefore able to satisfy the development of more advanced vibro-acoustic approaches for manifold surfaces in the future. Instead, in

---

[14] Like in a single traditional sensor, e.g. an accelerometer, it depends on the acquisition parameters, like frequency range, number of averages and spectral spacing, but now, as said in Section 2.1, for the synchronous acquisition of all dofs.

[79] the acclaimed SLDV showed to be a less field-wise reliable source for *direct vibro-acoustics*, due to sometime heavy and distorting noise patterns in the *receptance's fields*, which spread onto the acoustic mesh, affecting the simulations. Thanks to its intrinsic higher measurement quality in the *receptances*, only ESPI can, according to the author's experience and knowledge of reduced datasets in vibro-acoustics [76–78], achieve even better detailed results than DIC, but with the strong drawback of the much longer/expensive acquisition, processing requirements and laboratory-based set-up needed, whereas DIC can work in harsher environments with less demanding testing sessions.

Section 3.5 demonstrated that the proposed basic *pseudo-inverse full-field acoustic-vibrational FRFs* $V_{fa}^+(\omega)$ can be reliably evaluated from DIC-based high-resolution datasets, within the limits of the formulation in Eq. (9) when using $N_f = 1$. Later, Section 3.6 used what previously obtained to achieve the estimation of the force $\hat{F}_f(\omega)$ that the pressure field can concentrate on the sensed location of the shaker's head. In particular, the assessment of the very limited errors – in the order of the computational machine precision – in the pseudo-inverse force identification, by means of $Err_{F_f}(\omega)$ (Eq. (10)), showed the accuracy of the whole direct and pseudo-inverse procedure, independently of the excitation used, but achieved thanks to the rigorous $\mathbb{C}$ formulation. As continuously stressed throughout the whole paper, a key-aspect in ob-

taining good results is certainly the proper numerical handling of the $\mathbb{C}$ datasets, in every step of the formulation, processing and representation, by means of the custom C-language coding, OpenMP (parallelisation) and OpenGL (graphics) libraries.

The rationale of both Sections 3.5-3.6 lays in the will to explore a DIC-based *pseudo-inverse vibro-acoustics* procedure, which is able to estimate broad frequency band $\mathbb{C}$ forces on structures from airborne pressure fields. The latter need to be obtained in other tests or simulated, which are not part of this paper, as suggested in Section 3.8. Once these forces are obtainable, the further step will be to use them to evaluate – with the tools already developed by the author in [70,72,75] – the strain-stress distributions that are output on lightweight structures by airborne pressure excitation and that may cause fatigue damage and accelerated disruptions.

The clear lesson, learned from all the above mentioned simulations and validations, is that *native* full-field techniques, such as high-speed DIC in acquisitions with limited noise, when used with properly formulated $\mathbb{C}$ approaches, can be a valid alternative to numerical structural models and experimental modal models, also in vibro-acoustics, by retaining the closer linearised real-life representation of the structural behaviour.
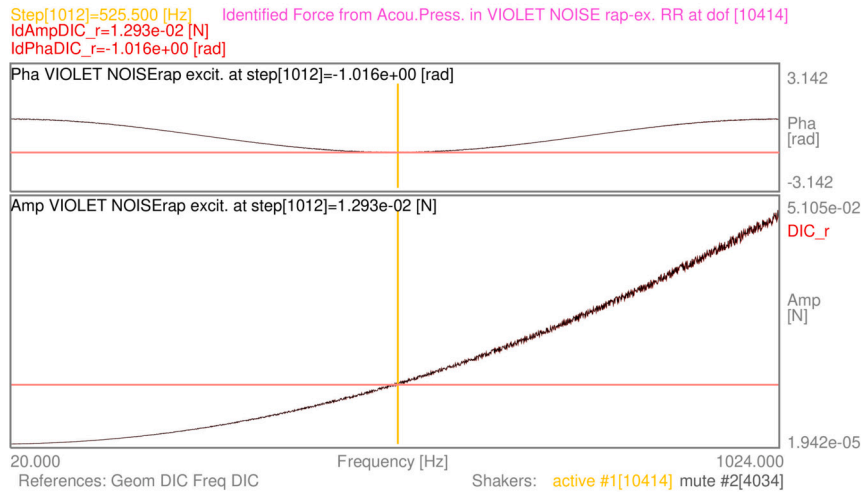
Fig. 23. Example of *identified force* $\hat{F}_{S1}(\omega)$ (in red) in the spectrum graph, evaluated against the *violet noise-rap* force (in black) in shaker 1, which originated the whole airborne acoustic pressure field.

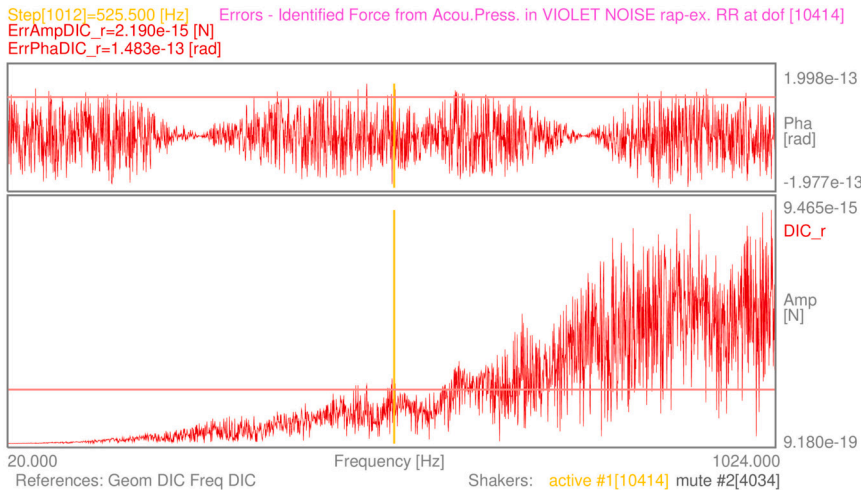**Fig. 24.** Errors $Err_{F_{S1}}(\omega)$ of the *identified force* $\hat{F}_{S1}(\omega)$ in the spectrum graph, while a *violet noise-rap* force in shaker 1 was the origin of the whole airborne acoustic pressure field.

Table 4

Summary of the computational errors in the *complex amplitude* of force identification from airborne acoustic pressure fields.

Noise colour	min Amp $Err_{F_{S1}}$ [N]	max Amp $Err_{F_{S1}}$ [N]	min Amp $\hat{F}_{S1}$ [N]	max Amp $\hat{F}_{S1}$ [N]	min Amp $Err_{F_{S1}}$ / min Amp $\hat{F}_{S1}$	max Amp $Err_{F_{S1}}$ / max Amp $\hat{F}_{S1}$
blue-std	5.624e-19	1.018e-14	4.886e-05	5.000e-02	1.151e-14	2.036e-13
pink-sp	3.610e-18	8.696e-15	4.886e-05	5.000e-02	7.388e-14	1.739e-13
red-ra	3.391e-20	8.486e-15	9.495e-07	5.087e-02	3.571e-14	1.668e-13
violet-rap	9.180e-19	9.465e-15	1.942e-05	5.105e-02	4.727e-14	1.854e-13

Table 5

Summary of the computational errors in the *complex phase* of force identification from airborne acoustic pressure fields.

Noise colour	min Pha $Err_{F_{S1}}$ [rad]	max Pha $Err_{F_{S1}}$ [rad]	min Pha $\hat{F}_{S1}$ [rad]	max Pha $\hat{F}_{S1}$ [rad]	min Pha $Err_{F_{S1}}$ / min Pha $\hat{F}_{S1}$	max Pha $Err_{F_{S1}}$ / max Pha $\hat{F}_{S1}$
blue-std	-1.126e-14	7.728e-15	-1.0(null)	1.0(null)	1.126e-14	7.728e-15
pink-sp	-2.134e-13	1.913e-13	-1.000	1.000	2.134e-13	1.913e-13
red-ra	-8.112e-15	1.544e-14	-1.0(null)	1.0(null)	8.112e-15	1.544e-14
violet-rap	-1.977e-13	1.998e-13	-1.024	1.024	1.931e-13	1.951e-13

3.8. Validation outlook

Future testing and researches – e.g., in pressurised climatic and anechoic chambers – are needed for a comprehensive proof of the highlighted procedure, before the whole methodology can find broad applicability to more complex structural parts, taking into account also the climatic variables for air, materials and boundary conditions under test.

Apart from the full-field structural vibration testing as in Section 2.1, in order to finely tune this approach, acoustic measurements – e.g., like those in [1,2,105–109] – are suggested, for future works, to characterise $p(a_a, \omega)$, once radiated by the vibrating plate. In the direct vibro-acoustic characterisation at the specific selected conditions, a relatively coarse microphone array can be used, to avoid acoustic distortions due to each microphone housing and fixing. Like in acoustic beamforming measurements [110], the microphone array might be moved parallel to the undeformed plate, by fractions of the array spacing, to enhance/oversample the spatial description of $p(a_a, \omega)$ and of $V_{af}(\omega)$ in Eq. (7) as desired. In the indirect path, a distributed noise source might be obtained by lumped sound emitters, like volume velocity sources (see in [105]) or calibrated loud speakers, positioned at known distances from the same microphone array and the flexible plate, again to assess and measure the distributed pressure fields $\hat{p}(a_a, \omega)$ with the wanted spatial resolution in the acoustic mesh selected as in Section 3.1. The $\hat{p}(a_a, \omega)$ might be investigated by the same shifting microphone array, in order to increase the acoustic dofs' density for tighter wavelength sampling, and come close to the high-spatial resolution in the mesh as here simulated, useful for the advances in camera electronics to come. Once properly calibrated as airborne excitation fields, the same sound sources should be run without the interposition of the slightly distorting microphone array, for a contactless and airborne excitation of the restrained plate. As in this paper, impedance heads might be used in the same structural interfaces with the shakers' excitations, to sense the transmitted forces in *direct* and *pseudo-inverse vibro-acoustic* testing. The sensed forces are vital to estimate the structure's linearisation in the *ebffr* and $V_{af}(\omega)$, in order to replicate the same broad frequency band dynamics with the shaker excitation; they are vital to measure $\hat{F}_f(\omega)$ from the airborne excitation, the former to be paired with $\hat{p}(a_a, \omega)$ for the tuning of $V_{fa}^+(\omega)$ in Eq. (8).

4. Conclusions

This work has comprehensively demonstrated, by means of a simple sound diffusion approach, the suitability for *direct* and *pseudo-inverse vibro-acoustic* analyses of DIC-based *full-field receptances*, which have relevant mapping ability, in both spatial and frequency domains. Attention was focused on the steps to obtain high-quality DIC-based datasets. Great accuracy was shown in fully retaining, by means of extensive *complex-valued* formulation in each step, the real-life structural dynamics of the radiating surface without hard-to-tune virtual modelling. No specific simplifications were needed, nor residual errors came from any modal identification. *Vibro-acoustic transfer matrices* and *acoustic pressure fields* were accurately obtained under the Rayleigh integral approximation and its *basic pseudo-inverse*, in order to retrieve the *complex-valued force* induced, by airborne acoustic pressure fields, on the vibrating plate, with the assessment of the computational errors in the procedure.

This paper highlights the possibility to retrieve structural excitations from airborne acoustic pressure fields and *experiment-based full-field receptances* with minimal relative errors, tracing future scenarios for extended research in NVH, coupled fluid-structural dynamics and fatigue-life predictions. The obtained achievements can be seen also as relevant advancements of vibro-acoustic experimental benchmarks for design procedures of structures with complex dynamic deformation patterns, and for advanced hybrid virtual prototyping, in aerospace and vehicle engineering.

CRediT authorship contribution statement

Alessandro Zanarini: Writing – review & editing, Writing – original draft, Visualization, Validation, Supervision, Software, Resources, Project administration, Methodology, Investigation, Funding acquisition, Formal analysis, Data curation, Conceptualization.

Declaration of competing interest

The author declares that he has no known competing financial interests or personal relationships that could have appeared to influence the work reported in this paper.

Acknowledgements

datasets and code the acoustic radiation was provided by the researcher out of his own savings. Professor Roberta Mullini is wholeheartedly acknowledged for her care in the English proofreading of the text.

References

[1] J.D. Maynard, E.G. Williams, Y. Lee, Nearfield acoustic holography: I. Theory of generalized holography and the development of NAH, J. Acoust. Soc. Am. 78 (4) (1985) 1395–1413, https://doi.org/10.1121/1.392911.

[2] W.A. Veronesi, J.D. Maynard, Nearfield acoustic holography (NAH) II. Holographic reconstruction algorithms and computer implementation, J. Acoust. Soc. Am. 81 (5) (1987) 1307–1322, https://doi.org/10.1121/1.394536.

[3] S. Kirkup, Computational solution of the acoustic field surrounding a baffled panel by the Rayleigh integral method, Appl. Math. Model. 18 (7) (1994) 403–407, https://doi.org/10.1016/0307-904X(94)90227-5.

[4] F. Augusztinovicz, P. Sas, F. Penne, Physical and numerical simulation of the performance of close-fitting partial engine shields, in: Proceedings of the Fortschritte der Akustik, 1995, pp. 475–478, https://last.hit.bme.hu/download/fulop/Publikaciok/DAGA96_EngShield.pdf.

[5] F. Augusztinovicz, F. Penne, P. Sas, Calculation of sound radiation from sources, characterized by the equivalent power volume velocity method, in: Proceedings of the 2nd Worldwide SYSNOISE Users Meeting, 1995, pp. 1–9, https://last.hit.bme.hu/download/fulop/Publikaciok/2ndSYSUsrMtg-EPVV.pdf.

[6] E.G. Williams, Fourier Acoustics: Sound Radiation and Nearfield Acoustical Holography, Elsevier Science, Amsterdam, The Netherlands, ISBN 978-0-12-753960-7, 1999, https://doi.org/10.1016/B978-0-12-753960-7.X5000-1.

[7] F. Gérard, M. Tournour, N. Masri, L. Cremers, M. Felice, A. Selmane, Acoustic transfer vectors for numerical modeling of engine noise, Sound Vib. 36 (2002) 20–25, http://www.sandv.com/downloads/0207gera.pdf.

[8] F. Fahy, Foundations of Engineering Acoustics, Academic Press, London, ISBN 978-0-12-247665-5, 2003, https://doi.org/10.1016/B978-0-12-247665-5.X5000-0.

[9] W. Desmet, Boundary element method in acoustics, Tech. Rep., Katholieke Universiteit Leuven, Belgium, Mechanical Engineering Department, Noise & Vibration research group, https://www.mech.kuleuven.be/en/research/, in: ISAAC 15 - Course on Numerical and Applied Acoustics, Katholieke Universiteit Leuven, Belgium, 2004, Mechanical Engineering Department, Noise & Vibration research group, https://www.isma-isaac.be.

[10] S. Kirkup, A. Thompson, Computing the acoustic field of a radiating cavity by the boundary element - Rayleigh integral method (BERIM), in: S.I. Ao, L. Gelman, D.W.L. Hukins, A. Hunter, A.M. Korsunsky (Eds.), World Congress on Engineering, WCE 2007, London, UK, July 2-4, 2007, in: Lecture Notes in Engineering and Computer Science, Newswood Limited, 2007, pp. 1401–1406, http://www.kirkup.info/publications/SKAT07.pdf, 2007.

[11] J.P. Arenas, Numerical computation of the sound radiation from a planar baffled vibrating surface, J. Comput. Acoust. 16 (03) (2008) 321–341, https://doi.org/10.1142/S0218396X08003671.

[12] M. Arunkumar, J. Pitchaimani, K. Gangadharan, M. Leninbabu, Vibro-acoustic response and sound transmission loss characteristics of truss core sandwich panel filled with foam, Aerosp. Sci. Technol. 78 (2018) 1–11, https://doi.org/10.1016/j.ast.2018.03.029.

[13] S. Kirkup, The boundary element method in acoustics: a survey, Appl. Sci. 9 (8) (2019), https://doi.org/10.3390/app9081642.

[14] M. Lesoinne, M. Sarkis, U. Hetmaniuk, C. Farhat, A linearized method for the frequency analysis of three-dimensional fluid/structure interaction problems in all flow regimes, in: Advances in Computational Methods for Fluid-Structure Interaction, Comput. Methods Appl. Mech. Eng. 190 (24) (2001) 3121–3146, https://doi.org/10.1016/S0045-7825(00)00385-6.

[15] G. Sandberg, P.-A. Wernberg, P. Davidsson, Fundamentals of Fluid-Structure Interaction, vol. 505, Springer Vienna, Vienna, 2009, pp. 23–101, Ch. 2, https://doi.org/10.1007/978-3-211-89651-8_2.

[16] R. Ohayon, C. Soize, Advanced computational dissipative structural acoustics and fluid-structure interaction in low- and medium-frequency domains. Reduced-order models and uncertainty quantification, Int. J. Aeronaut. Space Sci. 13 (2) (2012) 127–153, https://doi.org/10.5139/IJASS.2012.13.2.127.

[17] W. Vicente, R. Picelli, R. Pavanello, Y. Xie, Topology optimization of frequency responses of fluid–structure interaction systems, Finite Elem. Anal. Des. 98 (2015) 1–13, https://doi.org/10.1016/j.finel.2015.01.009.

[18] Q. Zhou, D. feng Li, A. Da Ronch, G. Chen, Y. ming Li, Computational fluid dynamics-based transonic flutter suppression with control delay, J. Fluids Struct. 66 (2016) 183–206, https://doi.org/10.1016/j.jfluidstructs.2016.07.002.

[19] E.H. Dowell, K.C. Hall, Modeling of fluid-structure interaction, Annu. Rev. Fluid Mech. 33 (2001) 445–490, https://doi.org/10.1146/annurev.fluid.33.1.445.

[20] R. Kamakoti, W. Shyy, Fluid–structure interaction for aeroelastic applications, Prog. Aerosp. Sci. 40 (8) (2004) 535–558, https://doi.org/10.1016/j.paerosci.2005.01.001.

[21] N. Werter, R. De Breuker, A novel dynamic aeroelastic framework for aeroelastic tailoring and structural optimisation, Compos. Struct. 158 (2016) 369–386, https://doi.org/10.1016/j.compstruct.2016.09.044.

[22] D. Li, Q. Zhou, G. Chen, Y. Li, Structural dynamic reanalysis method for transonic aeroelastic analysis with global structural modifications, J. Fluids Struct. 74 (2017) 306–320, https://doi.org/10.1016/j.jfluidstructs.2017.06.004.

[23] D. Li, A. Da Ronch, G. Chen, Y. Li, Aeroelastic global structural optimization using an efficient CFD-based reduced order model, Aerosp. Sci. Technol. 94 (2019) 105354, https://doi.org/10.1016/j.ast.2019.105354.

[24] Z. Chen, Y. Zhao, R. Huang, Parametric reduced-order modeling of unsteady aerodynamics for hypersonic vehicles, Aerosp. Sci. Technol. 87 (2019) 1–14, https://doi.org/10.1016/j.ast.2019.01.035.

[25] W. Tian, Y. Gu, H. Liu, X. Wang, Z. Yang, Y. Li, P. Li, Nonlinear aeroservoelastic analysis of a supersonic aircraft with control fin free-play by component mode synthesis technique, J. Sound Vib. 493 (2021) 115835, https://doi.org/10.1016/j.jsv.2020.115835.

[26] X. Wang, Z. Yang, S. Zhou, G. Zhang, Complex damping influences on the oscillatory/static instability characteristics of heated panels in supersonic airflow, Mech. Syst. Signal Process. 165 (2022) 108369, https://doi.org/10.1016/j.ymssp.2021.108369.

[27] H.H. Patil, J. Pitchaimani, Sound radiation characteristics of a beam under supersonic airflow and non-uniform temperature field, Aerosp. Sci. Technol. 147 (2024) 109001, https://doi.org/10.1016/j.ast.2024.109001.

[28] W. Heylen, S. Lammens, P. Sas, Modal Analysis Theory and Testing, 2nd edition, Katholieke Universiteit Leuven, Leuven, Belgium, ISBN 90-73802-61-X, 1998.

[29] D.J. Ewins, Modal Testing - Theory, Practicce and Application, 2nd edition, Research Studies Press Ltd., Baldock, Hertfordshire, England, ISBN 978-0-863-80218-8, 2000, https://www.wiley.com/en-it/Modal+Testing%3A+Theory%2C+Practice+and+Application%2C+2nd+Edition-p-9780863802188.

[30] B. Wu, Q. Wang, H. Liao, Y. Li, M. Li, Flutter derivatives of a flat plate section and analysis of flutter instability at various wind angles of attack, J. Wind Eng. Ind. Aerodyn. 196 (2020) 104046, https://doi.org/10.1016/j.jweia.2019.104046.

[31] C. Mendez, S. Le Clainche, R. Moreno-Ramos, J.M. Vega, A new automatic, very efficient method for the analysis of flight flutter testing data, Aerosp. Sci. Technol. 114 (2021) 106749, https://doi.org/10.1016/j.ast.2021.106749.

[32] F. Xu, J. Yang, M. Zhang, H. Yu, Experimental investigations on post-flutter performance of a bridge deck sectional model using a novel testing device, J. Wind Eng. Ind. Aerodyn. 217 (2021) 104752, https://doi.org/10.1016/j.jweia.2021.104752.

[33] G.C. Silva, M.V. Donadon, F.J. Silvestre, Experimental and numerical investigations on the nonlinear aeroelastic behavior of high aspect-ratio wings for different chord-wise store positions under stall and follower aerodynamic load models, Int. J. Non-Linear Mech. 131 (2021) 103685, https://doi.org/10.1016/j.ijnonlinmec.2021.103685.

[34] N. Tsushima, M. Tamayama, H. Arizono, K. Makihara, Geometrically nonlinear aeroelastic characteristics of highly flexible wing fabricated by additive manufacturing, Aerosp. Sci. Technol. 117 (2021) 106923, https://doi.org/10.1016/j.ast.2021.106923.

[35] N. Tsushima, W. Su, H. Gutierrez, M.G. Wolf, E.D. Griffin, J.T. Whittaker, M.P. Dumoulin, Monitoring multi-axial vibrations of flexible rockets using sensor-instrumented reference strain structures, Aerosp. Sci. Technol. 71 (2017) 285–298, https://doi.org/10.1016/j.ast.2017.09.026.

[36] Y. Liu, Y. Chen, C. Shao, A.M. Alshamrani, The efficient data-driven solution to estimate the nonlinear bending of sandwich doubly curved panel subjected to transient loading, Aerosp. Sci. Technol. 147 (2024) 108980, https://doi.org/10.1016/j.ast.2024.108980.

[37] D.D. Bueno, L.C.S. Góes, P.J.P. Gonçalves, Flutter analysis including structural uncertainties, Meccanica 50 (2015) 2093–2101, https://doi.org/10.1007/s11012-015-0138-8.

[38] X. Chen, Z. Qiu, X. Wang, Y. Li, R. Wang, Uncertain reduced-order modeling for unsteady aerodynamics with interval parameters and its application on robust flutter boundary prediction, Aerosp. Sci. Technol. 71 (2017) 214–230, https://doi.org/10.1016/j.ast.2017.09.018.

[39] M. Lokatt, Aeroelastic flutter analysis considering modeling uncertainties, J. Fluids Struct. 74 (2017) 247–262, https://doi.org/10.1016/j.jfluidstructs.2017.06.017.

[40] K. Tian, Y. Wang, D. Cao, K. Yu, Approximate global mode method for flutter analysis of folding wings, Int. J. Mech. Sci. 265 (2024) 108902, https://doi.org/10.1016/j.ijmecsci.2023.108902.

[41] A. Takezawa, M. Daifuku, Y. Nakano, K. Nakagawa, T. Yamamoto, M. Kitamura, Topology optimization of damping material for reducing resonance response based on complex dynamic compliance, J. Sound Vib. 365 (2016) 230–243, https://doi.org/10.1016/j.jsv.2015.11.045.

[42] F. Afonso, J. Vale, Éder Oliveira, F. Lau, A. Suleman, A review on non-linear aeroelasticity of high aspect-ratio wings, Prog. Aerosp. Sci. 89 (2017) 40–57, https://doi.org/10.1016/j.paerosci.2016.12.004.

[43] A. Abdelkefi, Aeroelastic energy harvesting: a review, Int. J. Eng. Sci. 100 (2016) 112–135, https://doi.org/10.1016/j.ijengsci.2015.10.006.

[44] M. Friswell, J.E. Mottershead, Finite Element Model Updating in Structural Dynamics, Solid Mechanics and Its Applications, Kuwler Academic Publishers, Springer Netherlands, ISBN 978-0-7923-3431-6, 1995, https://link.springer.com/book/10.1007/978-94-015-8508-8.

[45] A. Calvi, Uncertainty-based loads analysis for spacecraft: finite element model validation and dynamic responses, in: Uncertainties in Structural Mechanics and Analysis–Computational Methods, Comput. Struct. 83 (14) (2005) 1103–1112, https://doi.org/10.1016/j.compstruc.2004.11.019.

[46] A. Zanarini, Full field optical measurements in experimental modal analysis and model updating, J. Sound Vib. 442 (2019) 817–842, https://doi.org/10.1016/j.jsv.2018.09.048.

[47] K. Wyckaert, F. Augusztinovicz, Experimental vibro-acoustical modal analysis: reflections on reciprocity and excitation strategy, in: Proceedings of the 13th International Modal Analysis Conference, 1995, p. 7, https://last.hit.bme.hu/download/fulop/Publikaciok/IMACXIII_Recip.pdf.

[48] K. Wyckaert, F. Augusztinovicz, P. Sas, Vibro-acoustical modal analysis: reciprocity, model symmetry and model validity, J. Acoust. Soc. Am. 100 (1996) 3172–3181, https://last.hit.bme.hu/download/fulop/Publikaciok/JASA_Recip.pdf.

[49] K. Janssens, A. Vecchio, H. Van der Auweraer, Synthesis and sound quality evaluation of exterior and interior aircraft noise, in: Aircraft Noise Reduction, Aerosp. Sci. Technol. 12 (1) (2008) 114–124, https://doi.org/10.1016/j.ast.2007.10.002.

[50] Y. Du, P.J. Morris, The separation of radiating and non-radiating near-field pressure fluctuations in supersonic jets, J. Sound Vib. 355 (2015) 172–187, https://doi.org/10.1016/j.jsv.2015.06.020.

[51] B. Aloufi, K. Behdinan, J. Zu, Theoretical vibro-acoustic modeling of acoustic noise transmission through aircraft windows, J. Sound Vib. 371 (2016) 344–369, https://doi.org/10.1016/j.jsv.2016.02.023.

[52] J.C. Ebeling, I.C. Bacon, T.P. Bates, S.D. Sommerfeldt, J.D. Blotter, Improved efficiency of vibration-based sound power computation through multi-layered radiation resistance matrix symmetry, JASA Express Lett. 2 (12) (2022) 125601, https://doi.org/10.1121/10.0015355.

[53] S. Liao, M. Zhu, Combined discrete Fourier transform method for azimuthal acoustic mode analysis, Aerosp. Sci. Technol. 147 (2024) 109029, https://doi.org/10.1016/j.ast.2024.109029.

[54] J.-P. Song, G.-L. She, M. Eltaher, Nonlinear aero-thermo-elastic flutter analysis of stiffened graphene platelets reinforced metal foams plates with initial geometric imperfection, Aerosp. Sci. Technol. 147 (2024) 109050, https://doi.org/10.1016/j.ast.2024.109050.

[55] N. Roozen, Q. Leclère, D. Urbán, T. Méndez Echenagucia, P. Block, M. Rychtáriková, C. Glorieux, Assessment of the airborne sound insulation from mobility vibration measurements; a hybrid experimental numerical approach, J. Sound Vib. 432 (2018) 680–698, https://doi.org/10.1016/j.jsv.2018.06.058.

[56] H. Van der Auweraer, B. Dierckx, C. Haberstok, R. Freymann, et al., Structural modelling of car panels using holographic modal analysis, in: Proc. of the 1999 Noise and Vibration Conference, Traverse City (MI), USA, vol. 3, 1999, pp. 1495–1506, SAE P-342, https://doi.org/10.4271/1999-01-1849.

[57] H. Van der Auweraer, H. Steinbichler, C. Haberstok, R. Freymann, D. Storer, Integration of pulsed-laser ESPI with spatial domain modal analysis: results from the SALOME project, in: Proc. of the 4th International Conference on Vibration Measurements by Laser Techniques: Advances and Applications, vol. 4072, SPIE, 2000, pp. 313–322, https://doi.org/10.1117/12.386741.

[58] T. Kreis, Handbook of Holographic Interferometry: Optical and Digital Methods, Wiley-VCH, Berlin, Germany, ISBN 9783527405466, 2004, https://doi.org/10.1002/3527604154.

[59] H. Van der Auweraer, H. Steinbichler, C. Haberstok, R. Freymann, D. Storer, V. Linet, Industrial Applications of Pulsed-Laser ESPI Vibration Analysis, in: Proc. of the XIX IMAC, Kissimmee, FL, USA, SEM, 2001, pp. 490–496, https://www.researchgate.net/publication/238246330_Industrial_Applications_of_Pulsed-Laser_ESPI_Vibration_Analysis.

[60] H. Van der Auweraer, H. Steinbichler, S. Vanlanduit, C. Haberstok, R. Freymann, D. Storer, V. Linet, Application of stroboscopic and pulsed-laser electronic speckle pattern interferometry (ESPI) to modal analysis problems, Meas. Sci. Technol. 13 (2002) 451–463, https://doi.org/10.1088/0957-0233/13/4/305.

[61] A. Zanarini, Broad frequency band full field measurements for advanced applications: point-wise comparisons between optical technologies, Mech. Syst. Signal Process. 98 (2018) 968–999, https://doi.org/10.1016/j.ymssp.2017.05.035.

[62] A. Zanarini, Competing optical instruments for the estimation of full field FRFs, Measurement 140 (2019) 100–119, https://doi.org/10.1016/j.measurement.2018.12.017.

[63] J. Baqersad, P. Poozesh, C. Niezrecki, P. Avitabile, Photogrammetry and optical methods in structural dynamics – a review, in: Full-Field, Non-contact Vibration Measurement Methods: Comparisons and Applications, Mech. Syst. Signal Process. 86 (2017) 17–34, https://doi.org/10.1016/j.ymssp.2016.02.011.

[64] W. Wang, J.E. Mottershead, A. Ihle, T. Siebert, H.R. Schubach, Finite element model updating from full-field vibration measurement using digital image correlation, J. Sound Vib. 330 (8) (2011) 1599–1620, https://doi.org/10.1016/j.jsv.2010.10.036.

[65] W. Wang, J. Mottershead, T. Siebert, A. Pipino, Frequency response functions of shape features from full-field vibration measurements using digital image correlation, Mech. Syst. Signal Process. 28 (2011) 333–347, https://doi.org/10.1016/j.ymssp.2011.11.023.

[66] B. LeBlanc, C. Niezrecki, P. Avitabile, J. Sherwood, J. Chen, Surface Stitching of a Wind Turbine Blade Using Digital Image Correlation, in: R. Allemang, J. De Clerck, C. Niezrecki, J. Blough (Eds.), Topics in Modal Analysis II, vol. 6, Springer New York, New York, NY, 2012, pp. 277–284, https://doi.org/10.1007/978-1-4614-2419-2_27.

[67] D.A. Ehrhardt, M.S. Allen, S. Yang, T.J. Beberniss, Full-field linear and nonlinear measurements using Continuous-Scan Laser Doppler Vibrometry and high speed three-dimensional Digital Image Correlation, Mech. Syst. Signal Process. 86 (Part B) (2017) 82–97, https://doi.org/10.1016/j.ymssp.2015.12.003.

[68] M.N. Helfrick, C. Niezrecki, P. Avitabile, T. Schmidt, 3D digital image correlation methods for full-field vibration measurement, Mech. Syst. Signal Process. 25 (3) (2011) 917–927, https://doi.org/10.1016/j.ymssp.2010.08.013.

[69] A. Zanarini, On the making of precise comparisons with optical full field technologies in NVH, in: ISMA2020 Including USD2020 - International Conference on Noise and Vibration Engineering, Leuven, Belgium, September 7-9, KU Leuven, in: Optical Methods and Computer Vision for Vibration Engineering, 2020, pp. 2293–2308, https://past.isma-isaac.be/downloads/isma2020/proceedings/Contribution_695_proceeding_3.pdf.

[70] A. Zanarini, Chasing the high-resolution mapping of rotational and strain FRFs as receptance processing from different full-field optical measuring technologies, Mech. Syst. Signal Process. 166 (2022) 108428, https://doi.org/10.1016/j.ymssp.2021.108428.

[71] A. Zanarini, About the excitation dependency of risk tolerance mapping in dynamically loaded structures, in: ISMA2022 Including USD2022 - International Conference on Noise and Vibration Engineering, Leuven, Belgium, September 12-14, KU Leuven, in: Structural Health Monitoring, 2022, pp. 3804–3818, https://past.isma-isaac.be/downloads/isma2022/proceedings/Contribution_208_proceeding_3.pdf.

[72] A. Zanarini, Introducing the concept of defect tolerance by fatigue spectral methods based on full-field frequency response function testing and dynamic excitation signature, Int. J. Fatigue 165 (2022) 107184, https://doi.org/10.1016/j.ijfatigue.2022.107184.

[73] A. Zanarini, Risk tolerance mapping in dynamically loaded structures as excitation dependency by means of full-field receptances, in: IMAC XLI - International Modal Analysis Conference - Keeping IMAC Weird: Traditional and Non-traditional Applications of Structural Dynamics, Conference Proceedings of the Society for Experimental Mechanics Series, Austin (Texas), USA, in: J. Baqersad, D. Di Maio (Eds.), Computer Vision & Laser Vibrometry, vol. 6, Springer Nature Switzerland AG & SEM Society for Experimental Mechanics, 2023, pp. 43–56, Chapter 9, https://doi.org/10.1007/978-3-031-34910-2_9.

[74] A. Zanarini, Exploiting DIC-based full-field receptances in mapping the defect acceptance for dynamically loaded components, in: The 5th International Conference on Structural Integrity, 28 August - 1 September, 2023, Proc. Struct. Integr. 54C (2024) 99–106, https://doi.org/10.1016/j.prostr.2024.01.061.

[75] A. Zanarini, Mapping the defect acceptance for dynamically loaded components by exploiting DIC-based full-field receptances, Eng. Fail. Anal. 163 (2024) 108385, https://doi.org/10.1016/j.engfailanal.2024.108385.

[76] A. Zanarini, On the approximation of sound radiation by means of experiment-based optical full-field receptances, in: ISMA2022 Including USD2022 - International Conference on Noise and Vibration Engineering, Leuven, Belgium, September 12-14, KU Leuven, in: Optical Methods, 2022, pp. 2735–2749, https://past.isma-isaac.be/downloads/isma2022/proceedings/Contribution_207_proceeding_3.pdf.

[77] A. Zanarini, Experiment-based optical full-field receptances in the approximation of sound radiation from a vibrating plate, in: IMAC XLI - International Modal Analysis Conference - Keeping IMAC Weird: Traditional and Non-traditional Applications of Structural Dynamics, Conference Proceedings of the Society for Experimental Mechanics Series, Austin (Texas), USA, in: J. Baqersad, D. Di Maio (Eds.), Computer Vision & Laser Vibrometry, vol. 6, Springer Nature Switzerland AG & SEM Society for Experimental Mechanics, 2023, pp. 1–13, Chapter 4, https://doi.org/10.1007/978-3-031-34910-2_4.

[78] A. Zanarini, On the use of full-field receptances in inverse vibro-acoustics for airborne structural radiation, in: The 5th International Conference on Structural Integrity, 28 August - 1 September, Proc. Struct. Integr. 54C (2024) 107–114, https://doi.org/10.1016/j.prostr.2024.01.062.

[79] A. Zanarini, On the influence of scattered errors over full-field receptances in the Rayleigh integral approximation of sound radiation from a vibrating plate, Acoustics 5 (2023) 948–986, https://doi.org/10.3390/acoustics5040055.

[80] W. Liu, D. Ewins, The importance assessment of RDOF in FRF coupling analysis, in: Proceedings of the IMAC 17th Conference, Kissimmee, Florida, Society for Experimental Mechanics (SEM), 1999, pp. 1481–1487, https://citeseerx.ist.psu.edu/document?repid=rep1&type=pdf&doi=c44ebc7b37f462e47b44aee1acb1f9de704e92d6.

[81] Research Network, QUATTRO Brite-Euram project no: BE 97-4184, Tech. Rep., European Commision Research Framework Programs, 1998.

[82] M. Haeussler, S. Klaassen, D. Rixen, Experimental twelve degree of freedom rubber isolator models for use in substructuring assemblies, J. Sound Vib. 474 (2020) 115253, https://doi.org/10.1016/j.jsv.2020.115253.

[83] J. Wind, Y. Wijnant, A. de Boer, Fast evaluation of the Rayleigh integral and applications to inverse acoustics, in: Proceedings of the ICSV13, The Thirteenth International Congress on Sound and Vibration, Vienna, Austria, July 2–6, 2006, International Institute of Acoustics (IIAV), 2006, pp. 1–8, https://research.utwente.nl/en/publications/fast-evaluation-of-the-rayleigh-integral-and-applications-to-inve.

[84] R. Citarella, L. Federico, A. Cicatiello, Modal acoustic transfer vector approach in a FEM-BEM vibro-acoustic analysis, Eng. Anal. Bound. Elem. 31 (3) (2007) 248–258, https://doi.org/10.1016/j.enganabound.2006.09.004.

[85] P. Mas, P. Sas, Acoustic source identification based on microphone array processing, Tech. Rep., Katholieke Universiteit Leuven, Belgium, Mechanical Engineering De-

partment, Noise & Vibration research group, 2004, https://www.mech.kuleuven.be/en/research/, in: ISAAC 15 - Course on Numerical and Applied Acoustics, Katholieke Universiteit Leuven, Belgium, 2004, Mechanical Engineering Department, Noise & Vibration research group, https://www.isma-isaac.be.

[86] Z. Zhang, A flexible new technique for camera calibration, IEEE Trans. Pattern Anal. Mach. Intell. 22 (11) (2000) 1330–1334, https://doi.org/10.1109/34.888718.

[87] J. Kannala, S. Brandt, A generic camera model and calibration method for conventional, wide-angle, and fish-eye lenses, IEEE Trans. Pattern Anal. Mach. Intell. 28 (8) (2006) 1335–1340, https://doi.org/10.1109/TPAMI.2006.153.

[88] A.E. Conrady, Decentred Lens-Systems, Mon. Not. R. Astron. Soc. 79 (5) (1919) 384–390, https://doi.org/10.1093/mnras/79.5.384.

[89] D. Brown, Decentering distortion of lenses, Photogramm. Eng. 32 (1966) 444–462, http://close-range.com/docs/Decentering_Distortion_of_Lenses_Brown_1966_may_444-462.pdf.

[90] J.I. Ronda, A. Valdés, Geometrical analysis of polynomial lens distortion models, J. Math. Imaging Vis. 61 (2019) 252–268, https://doi.org/10.1007/s10851-018-0833-x.

[91] V. Kibitkin, A. Solodushkin, V. Pleshanov, A. Napryushkin, On a choice of input parameters for calculation the vector field and deformation with DIC, Measurement 95 (2017) 266–272, https://doi.org/10.1016/j.measurement.2016.10.020.

[92] E.M.C. Jones, M.A. Iadicola (Eds.), A Good Practices Guide for Digital Image Correlation, International Digital Image Correlation Society, 2018, https://doi.org/10.32720/idics/gpg.ed1.

[93] P. Poozesh, A. Sarrafi, Z. Mao, P. Avitabile, C. Niezrecki, Feasibility of extracting operating shapes using phase-based motion magnification technique and stereophotogrammetry, J. Sound Vib. 407 (2017) 350–366, https://doi.org/10.1016/j.jsv.2017.06.003.

[94] P.F. Luo, Y.J. Chao, M.A. Sutton, W.H. Peters, Accurate measurement of three-dimensional deformations in deformable and rigid bodies using computer vision, Exp. Mech. 33 (1993) 123–132, https://doi.org/10.1007/BF02322488.

[95] M.A. Sutton, J.J. Orteu, H. Schreier, Image Correlation for Shape, Motion and Deformation Measurements: Basic Concepts, Theory and Applications, Springer US, ISBN 978-0-387-78746-6, 2009, https://doi.org/10.1007/978-0-387-78747-3.

[96] L.C. Michel Tournour, P. Guisset, F. Augusztinovicz, F. Marki, Inverse numerical acoustics based on acoustic transfer vectors, in: Proc. of 7th International Congress on Sound and Vibration - ICSV7, 2000, pp. 2069–2076, https://last.hit.bme.hu/download/fulop/Publikaciok/ICSV7_Inverse.pdf.

[97] S. Khoo, Z. Ismail, K. Kong, Z. Ong, S. Noroozi, W. Chong, A. Rahman, Impact force identification with pseudo-inverse method on a lightweight structure for under-determined, even-determined and over-determined cases, Int. J. Impact Eng. 63 (2014) 52–62, https://doi.org/10.1016/j.ijimpeng.2013.08.005.

[98] W.H. Press, S.A. Teukolsky, W.T. Vetterling, B.P. Flannery, Numerical Recipes in C: The Art of Scientific Computing, 2nd edition, Cambridge Univ. Press, England, 1992, http://numerical.recipes.

[99] L. Eldén, A weighted pseudoinverse, generalized singular values, and constrained least squares problems, BIT Numer. Math. 22 (1982) 487–502, https://doi.org/10.1007/BF01934412.

[100] P. Guillaume, E. Parloo, G. De Sitter, Source identification from noisy response measurements using an iterative weighted pseudo-inverse approach, in: Proceedings of the 2002 International Conference on Noise and Vibration Engineering, ISMA, 2002, pp. 1817–1824, https://past.isma-isaac.be/isma2002/.

[101] S. Zheng, L. Zhou, X. Lian, K. Li, Technical note: Coherence analysis of the transfer function for dynamic force identification, Mech. Syst. Signal Process. 25 (6) (2011) 2229–2240, https://doi.org/10.1016/j.ymssp.2011.01.015.

[102] S. Vanlanduit, P. Guillaume, B. Cauberghe, E. Parloo, G. De Sitter, P. Verboven, On-line identification of operational loads using exogenous inputs, J. Sound Vib. 285 (1) (2005) 267–279, https://doi.org/10.1016/j.jsv.2004.08.028.

[103] S.K. Sen, R.P. Agarwal, 3 - History of zero including its representation and role, in: S.K. Sen, R.P. Agarwal (Eds.), Zero, Academic Press, 2016, pp. 29–75, https://doi.org/10.1016/B978-0-08-100774-7.00003-X.

[104] Wikipedia.org, Machine epsilon, 2024, https://en.wikipedia.org/wiki/Machine_epsilon. (Accessed 18 April 2024).

[105] A. Zanarini, F. De Coninck, K. Mendrok, P. Sas, Direct and indirect vibro-acoustic measurements for road noise NVH predictions, in: Proceedings of the IDETC/CIE ASME International Design Engineering Technical Conferences & Computers and Information in Engineering Conference, Long Beach, California, USA, September 24-28, ASME, 2005, pp. 353–361, Paper DETC2005-85633, https://doi.org/10.1115/DETC2005-85633.

[106] C. Coster, D. Nagahata, P.J.G. van der Linden, On the accuracy reciprocal and direct vibro-acoustic transfer-function measurements on vehicles for lower and medium frequencies, in: Proceedings of the 24th International Conference on Noise and Vibration Engineering (ISMA2010) Conference, 2010, pp. 3873–3886, https://past.isma-isaac.be/downloads/isma2010/papers/isma2010_0243.pdf.

[107] G. Squicciarini, A. Putra, D.J. Thompson, X. Zhang, M.A. Salim, Use of a reciprocity technique to measure the radiation efficiency of a vibrating structure, Appl. Acoust. 89 (2015) 107–121, https://doi.org/10.1016/j.apacoust.2014.09.013.

[108] P. Wagner, A.P. Huesmann, M.V. van der Seijs, Application of dynamic substructuring in NVH design of electric drivetrains, in: Proceedings of the ISMA2020 Including USD2020 - International Conference on Noise and Vibration Engineering, Leuven, Belgium, September 7-9, in: Vehicle Noise and Vibration (NVH), KU Leuven, 2020, pp. 3365–3382, https://past.isma-isaac.be/downloads/isma2020/proceedings/Contribution_369_proceeding_3.pdf.

[109] J. Ortega Almirón, F. Bianciardi, P. Corbeels, N. Pieroni, P. Kindt, W. Desmet, Vehicle road noise prediction using component-based transfer path analysis from tire test-rig measurements on a rolling tire, J. Sound Vib. 523 (2022) 116694, https://doi.org/10.1016/j.jsv.2021.116694.

[110] P. Castellini, M. Martarelli, Acoustic beamforming: Analysis of uncertainty and metrological performances, Mech. Syst. Signal Process. 22 (3) (2008) 672–692, https://doi.org/10.1016/j.ymssp.2007.09.017.